Complex evolution of Holocene hydroclimate, fire and vegetation revealed by molecular, minerogenic and biogenic proxies, Marais Geluk wetland, eastern Free State, South Africa

Sjöström, J.K.; Martínez Cortizas, A.; Nylund, A.; Hardman, A.; Kaal, J.; Smittenberg, R.H.; Risberg, J.; Schillereff, D.; Norström, E.

DOI:
10.1016/j.quascirev.2023.108216

Quaternary Science Reviews 314 (2023) 108216

Contents lists available at ScienceDirect

Quaternary Science Reviews

journal homepage: www.elsevier.com/locate/quascirev

Complex evolution of Holocene hydroclimate, fire and vegetation revealed by molecular, minerogenic and biogenic proxies, Marais Geluk wetland, eastern Free State, South Africa

J.K. Sjöström [a,b,c,*], A. Martínez Cortizas [c,d], A. Nylund [b,c], A. Hardman [e], J. Kaal [f], R.H. Smittenberg [b,c], J. Risberg [a], D. Schillereff [g], E. Norström [a,b]

[a] Dept of Physical Geography, Stockholm University, Stockholm, Sweden
[b] Dept of Geological Sciences, Stockholm University, Stockholm, Sweden
[c] Bert Bolin Centre For Climate Research, Stockholm University, Stockholm, Sweden
[d] EcoPast (GI-1553), Universidad de Santiago de Compostela, Santiago de Compostela, Spain
[e] Department of Earth Sciences, University of Birmingham, Birmingham, United Kingdom
[f] Pyrolyscience SLU, 15706 Santiago de Compostela, Spain
[g] King's College, London, United Kingdom

ARTICLE INFO

Handling Editor: P Rioual

Keywords:
Hydroclimate
Paleofire
South Africa
FTIR
CS-XRF
Phytoliths
Geochemistry
Holocene
Multiproxy
Pyrolysis-GC-MS

ABSTRACT

The Holocene climate history of Southern Africa remains inconclusive despite the increasing number of proxy records from the region. This might be related to the diversity of proxy records, how the proxies are interpreted, or that proxies may respond to more than one forcing (e.g. hydroclimate, fire, temperature.). Here, a 175-cm peat sequence from Free State, South Africa (28°17′53″S, 29°25′10.9″E), was analyzed using a comprehensive set of novel and conventional proxies, including isotopic ($\delta^{13}C$), elemental (CS-XRF), mineral (pXRD), molecular (FTIR-ATR and pyrolysis-GC-MS), grain size (Malvern 3000) and GSSC phytolith composition. The chronology was constructed through AMS radiocarbon dating (n = 7). The early Holocene (10,380–7000 cal yr BP) was characterized by an initial wet phase, followed by relative dryness, at least seasonally, evidenced by slow accumulation rates, low organic content and dominance of terrestrial vegetation in the organic matter matrix. From 7000 cal yr BP, decreasing temperatures, as evidenced in regional climate reconstructions, were associated at Marias Geluk with higher biogenic silica and organic matter content and an increase of moisture-adapted grasses, indicating increasingly mesic conditions. This trend was amplified after 6000 cal yr BP, co-occurring with a southward displacement of the ITCZ. Complex proxy dynamics were observed between 4300 and 2180 cal yr BP, with bulk organic proxies indicating a drier environment (lower carbon content, slow accumulation rates, enriched $\delta^{13}C$ values) but the phytolith record pointing towards relatively mesic conditions. The period was also associated with increased fire frequency, that also reached the local wetland. We suggest that the period was associated with seasonally mesic conditions together with increased fire incidence, which affected some of the organic proxies. Increased fire activity was also recorded in the region, while the hydroclimatic indications differed. The last 2000 years, during which human activity is known to have increased in the region, was characterized by lower fire incidence and variable, but relatively moist, conditions. The hydroclimatic inferences for the last 2000 years are in line with previous studies from the region, but additional studies are needed to decipher if the decline in fire incidence was associated to climate forcings, human activities, or a combination of both. The multiproxy approach applied here - in particular the inclusion of FTIR-ATR and pyrolysis GC-MS - revealed a complex interplay between vegetation dynamics, hydrology and paleofire variability. This study confirms that relatively small Holocene temperature variations (compared to northern higher latitudes) were associated with major hydrological variability at Marais Geluk, and reinforces concerns from earlier studies that the hydroclimate of the region is vulnerable to climate change. The result s also show that the southward displacement of the ITCZ, and associated tropical air masses, likely had significant effects on regional hydrology and fire incidence.

* Corresponding author. Stockholm University, Dept. of Geological Sciences, S-106 91, Stockholm, Sweden.
E-mail address: jenny.sjostrom@geo.su.se (J.K. Sjöström).

https://doi.org/10.1016/j.quascirev.2023.108216
Received 6 April 2023; Received in revised form 3 July 2023; Accepted 4 July 2023
Available online 20 July 2023

1. Introduction

To date, southern Africa has experienced 1.04–1.44 °C warming since pre-industrial times (Trisos et al., 2022). The projected climate change in southern Africa, in a 1.5–2°C warming scenario, include increased frequency of heatwaves, decreasing mean annual rainfall and increasing evaporation leading to more intense drought conditions. Heavy rainfall events are projected to decrease in the western parts, while an increase is projected for the eastern parts (Trisos et al., 2022). However, some of these predictions are uncertain, and additional observational as well as paleo-climate data are needed to further understand the mechanisms governing hydroclimatic changes in the region (Trisos et al., 2022). Paleoclimatic studies, utilizing natural archives such as lakes or peat, can be used to infer hydroclimatic changes during past climatic variability, and aid in improving prediction capabilities.

Wetlands are relatively rare in South Africa, but somewhat more prevalent in the wetter, eastern parts of the summer rainfall region (Mucina and Rutherford, 2006). The existence of wetlands in sub-tropical settings is related to local positive water-balances. In eastern South Africa, wetlands typically occur in close proximity to rivers and streams that become impeded by bedrock, faulting, swelling soils or sedimentation, allowing peat accumulation. These streams and rivers may be either perennial, seasonal or ephemeral (Tooth and McCarthy, 2007). Moreover, southern African wetlands are characterized by seasonal desiccation and recurrent fires, leading to overall low organic matter (OM) accumulation (Tooth and McCarthy, 2007).

A chronostratigraphic review, compiling paleoclimatic inferences from several wetland studies in south-eastern Africa (Norström et al., 2021),

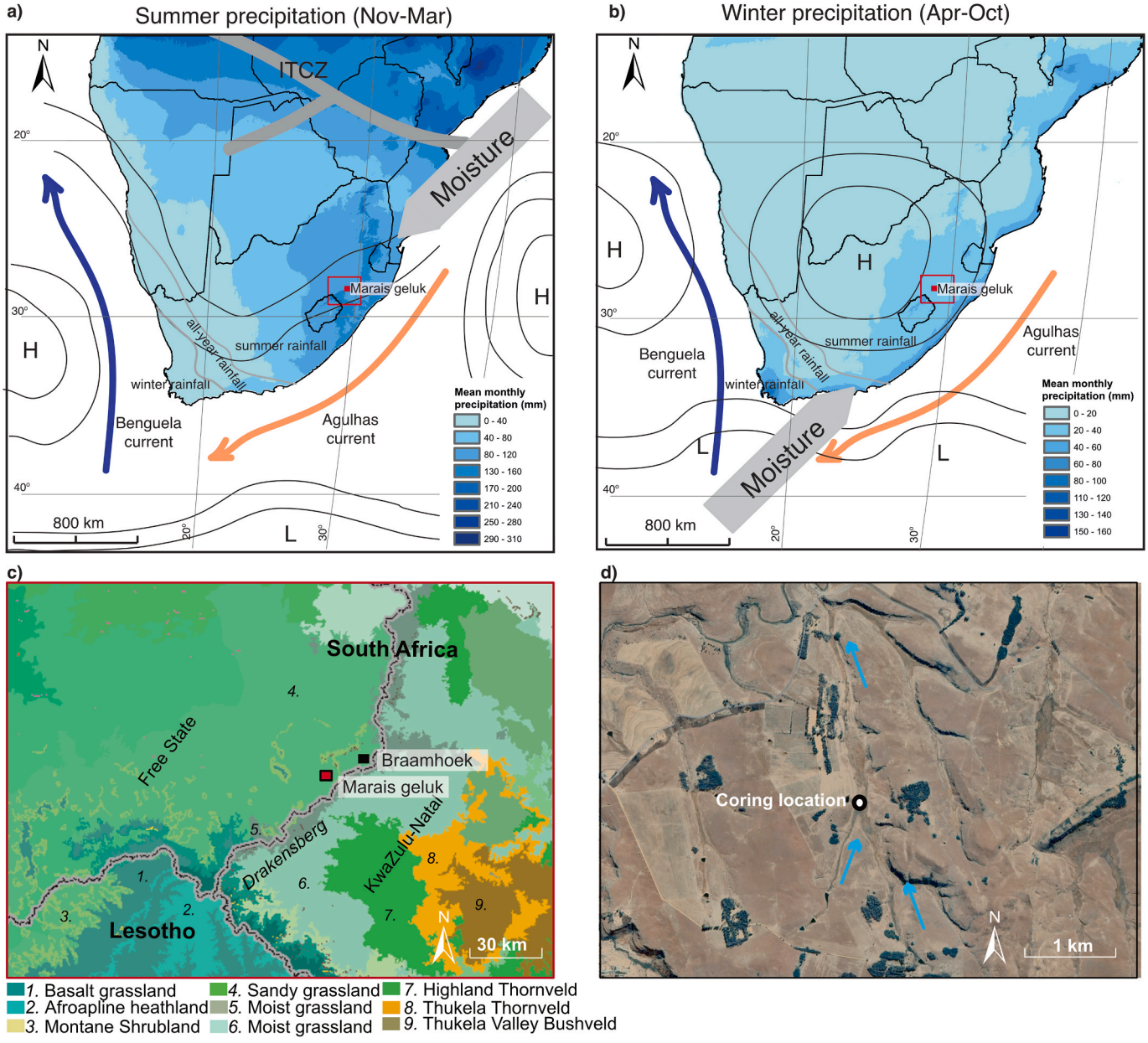

Fig. 1. Location map. **a)** Location of large-scale atmospheric systems affecting the region (ITCZ, major high and low air pressure systems) during summer precipitation (Nov–Mar), including major sources of moisture. Mean monthly precipitation indicated in blue shades. Major ocean currents are also indicated. The red box indicates the zoomed in area of panel c), while the red filled box marks the location of Marais Geluk wetland. **b)** Location of major atmospheric systems during winter (Apr–Oct) and monthly mean precipitation (blue shades). Moisture source shifted from north-east to south-west compared to summer. c) Vegetation zones and location of Marais Geluk (this study) and Braamhoek (previous studies), adapted from SANBI 2018 Vegetation map of South Africa, Lesotho and Swaziland. d) Satellite image of the study area, coring location and nearby streams. Adapted from Google Earth (2023).

found that several studies reported mesic conditions during the early Holocene (ca. 10.5–8 ka cal yr BP), but relatively dry conditions for the same period have also been inferred. For example, the Makapansgat stalagmite record (Holmgren et al., 2003) Wondercrater spring mound (Scott et al., 2003) and Verloren Valei wetland sequence (Breman et al. (2019) all report relatively dry conditions during the period. For the mid Holocene (ca. 8–4 ka cal yr BP), Breman et al. (2019) inferred mostly moist conditions, whereas Holmgren et al. (2003), Norström et al. (2009, 2014), Finné et al. (2010) inferred relative dryness. For the last 2000 years, greater hydroclimatic variability has been observed, with mostly mesic conditions (Norström et al., 2009, 2014; Finné et al., 2010; Sjöström et al., 2017; Breman et al., 2019; Combrink et al., 2022), while paleostudies from the Mfabeni wetland, in coastal south-eastern South Africa, reported relatively dry conditions (e.g. Finch and Hill, 2008; Miller et al., 2019; Fietz et al., 2023). This may be related to how the proxies are interpreted, that some proxies respond to more than one forcing, differences in sampling resolution, location of study site, and/or local factors affecting the individual study site. Here, we aim to bridge some of these knowledge gaps by analysing a 175-cm peat sequence for multiple proxies: near continuous CS-XRF (core scanner X-ray fluorescence), molecular FTIR-ATR (Fourier transform infra-red - attenuated total reflectance), pyrolysis-GC-MS (pyrolysis–gas-chromatography–mass spectrometry), carbon isotope analysis ($\delta^{13}C$) together with total organic carbon (TOC) and nitrogen (TN) analyses. These results are anchored by grain size, XRD (X-ray diffraction) mineral and grass silica short cell (GSSC) phytolith analyses. Our study site, Marais Geluk wetland, is located ca. 18 km west of Braamhoek (Fig. 1), a previously well-studied site (Finné et al., 2010; Norström et al., 2009, 2014). The Braamhoek proxy-record covers the last 16,000 cal yr BP, but with relatively low resolution during mid- and late-Holocene. Our record from Marais Geluk encompasses this period with higher resolution and may therefore provide data and improved understanding of a time period for which divergent trends have been recorded in previous paleo-studies (Norström et al., 2021, and references therein).

The vegetation in the study area consists of a mix of C_3 (mainly trees and shrubs) and C_4 (grasses) plants (Vogel et al., 1978), which means that $\delta^{13}C$ values are a suitable tool to track shifts been C_3 and C_4 vegetation through time (Norström et al., 2009). However, when analyzing bulk samples for $\delta^{13}C$ ($\delta^{13}C_{bulk}$) values interpreting discrete values may not be straightforward as the results can have strong local influences, particularly during periods of high productivity. Coupling $\delta^{13}C_{bulk}$ with additional analyses, like grass silica short cell (GSSC) phytolith analysis, can aid in untangling the local wetland signal from changes in the surrounding grassland. Fires can also affect the vegetation distribution, for example by suppressing some species (e.g. trees) and promoting others (grasses, bushes) (Cordova et al., 2019; Finch et al., 2022; Norström et al., 2009). In addition, studies have shown that organic proxies (e.g. C, $\delta^{13}C$, and other biomarkers) may be affected by fires (Krull et al., 2003; Sarangi et al., 2022; Turney et al., 2006). Here, we will explore whether FTIR, in combination with pyrolysis GC-MS, can be used to detect charcoal content, and in extent paleofire dynamics, in bulk wetland samples.

The loss on ignition (LOI), TOC and TN content provide information on total OM content, while C/N ratios may indicate the sources of the OM (e.g. aquatic or terrestrial) (Meyers, 1994; Meyers and Ishiwatar, 1993). CS-XRF allows non-destructive, near-continuous resolution of elemental downcore variability, enabling event markers to be detected at the millimeter-scale that might have been missed by coarser sub-sampling, and have become an increasingly common analytical approach for lacustrine and marine sediments (Croudace et al., 2019; Löwemark et al., 2019; Bertrand et al. submitted). CS-XRF analysis can be used to reconstruct past environmental changes such as paleofloods, productivity, variations of aeolian input and movement of the Intertropical Convergence Zone (ITCZ) (Brown et al., 2007; Kylander et al., 2011; Moreno et al., 2007, 2008; Yancheva et al., 2007). To date, peat cores have been less frequently analyzed, because the analysis requires flat surfaces and dense material (Bertrand et al. *submitted*), a pre-requisite that peat cores, especially from northern latitudes, do not always fulfill. Peat sequences from southern Africa are typically more decomposed, and thus more similar in terms of density and smoothness to a lacustrine sediment. To our knowledge, only a few peat sequences from southern Africa have been analyzed by CS-XRF (Humphries et al., 2020; Humphries, 2021; Kylander et al., 2021), and even fewer have combined it with FTIR-ATR analysis (Kylander et al., 2021). FTIR-ATR is a fast, non-destructive, analytical approach that records information on the vibration of molecular bonds (organic and inorganic) in the analyzed material. Information obtained via FTIR-ATR can be used to reconstruct past variations in decomposition, mineral composition and carbon compounds in peat bulk samples (Artz et al., 2006; Biester et al., 2014; Hodgkins et al., 2018; Kylander et al., 2021; Martínez Cortizas et al., 2021a, 2021b). Previous studies have shown that charcoal can be detected by FTIR-ATR (e.g. Guo and Bustin, 1998; Gosling et al., 2019). Here, we will evaluate whether FTIR-ATR analysis can detect charcoal in bulk wetland samples, and verify the results from FTIR-ATR by a secondary, independent analysis: pyrolysis-GC-MS. The high-resolution CS-XRF data (n = 431) will be combined with FTIR-ATR (n = 83), pyrolysis-GC-MS (n = 77), grain size (n = 19) and XRD mineral (n = 11) measurements to aid and anchor the interpretations.

The results will be explored with principal component analysis (PCA), which aims to reduce the number of dimensions of the multivariate datasets, thereby explaining as much of the variance as possible within few components (Davis, 2002). This may allow variables displaying similar behavior through a sequence, and thus may be controlled by the same process, to be identified.

The aims of this study are to: a) compare the responses of the different proxies analyzed and explore similarities and differences; b) reconstruct paleo hydroclimatic and vegetational changes throughout the studied period; and c) put the results into a regional paleoclimatic context.

1.1. Study area

The studied wetland (28°17′53″S, 29°25′10.9″E, 1700 m.a.s.l.) is located in the vicinity of Marais Geluk farm, north-eastern Free State, South Africa. The study area is located 4 km north-west of the Drakensberg escarpment (Fig. 1a and b). The altitudinal difference (~500 m) of the escarpment governs the separation of the high grassland biomes to the north-west, and the lowland grass and savannah biomes to the south-east (Fig. 1c). The wetland is located in an area where two streams converge (Fig. 1, d). The stream drains to the Wilge River 3 km north of the study area. The area surrounding the wetland is currently grazed by cattle, with the coring location protected by a fence to prevent cattle from entering the wettest parts. The contemporary wetland vegetation is dominated by sedges, whereas grasses dominate the surrounding hills. The study area belongs to the Sandy Grassland biome (Fig. 1, c), where a majority of grasses (75–95%.) use a C_4 photosynthetic pathway to fix CO_2 and 5–25% use a C_3 photosynthetic pathway (Mucina and Rutherford, 2006; South African National Biodiversity Institute, 2018; Vogel et al., 1978). Shrubs, trees and bushes use a C_3 photosynthetic pathway (Vogel et al., 1978). The bedrock of the area is dominated by sandstones of the Karoo supergroup and the Beaufort series that formed around 260 Ma ago, co-occurring with local intrusions of mudstones and shales (Holmes and Barker, 2006).

The climate of South Africa is governed by several large-scale processes such as the seasonal movement of the ITCZ, the circumpolar vortex over Antarctica and temperature contrasts between the warm Indian Ocean and the cooler Atlantic Ocean (Scott and Lee-Thorp, 2004) (Fig. 1). During austral summers, the summer rainfall region is dominated by warm and moist easterly air masses, associated with a southward shift of the ITCZ on the eastern side of the continent (Fig. 1, a). During austral winters, dry, high pressure conditions develop in the summer rainfall region, while cool and moist air masses, associated with expansion of the Antarctic circumpolar vortex, dominate in the

south-western Cape, causing dominantly winter rainfall (Fig. 1, b) (Scott and Lee-Thorp, 2004). The Marais Geluk wetland is located in the summer rainfall region, receiving ca. 1400 mm of rain annually, of which around 80% falls between October and March. Temperatures range from an average daily maximum of 27 °C (January) to −2 °C (June and July). Daily mean maximum temperature during the growing season (October–March) is 25 °C, while the mean minimum is 11 °C (South African Weather Bureau).

2. Methods

2.1. Fieldwork, subsampling and LOI analysis

In December 2011, four sediment cores were retrieved using a Russian corer equipped with a 50 × 5 cm chamber to a total depth of 175 cm. The cores were wrapped in plastic immediately after retrieval and put in half-cut PVC tubes. The cores were stored cold (4 °C) upon arrival at Stockholm University. The cores were sub-sampled at 1-cm resolution, and every other sample was freeze dried and milled to a fine powder in preparation for additional analyses (see below). LOI analysis followed Dean (1974), and included initial drying at 105 °C, weighing, and combustion at 550°C for 5 h, and weighing of the ash residue. LOI was calculated by subtracting the sample weight before and after combustion, and calculating the percentage weight lost.

2.2. AMS radiocarbon dating and chronology

Due to the absence of visible plant macro fossils throughout the sequence, bulk samples were used for radiocarbon dating (n = 7). The bulk samples were dissolved in distilled water and transferred to a petri dish, where root remains were removed using a pair of tweezers under a magnification lens, following Norström et al. (2014). Prior to analysis, the samples were soaked in 1% HCl to remove carbonates. The soluble part of the residue was precipitated by addition of 1% NaOH, and the precipitate used for AMS radiocarbon dating. Radiocarbon dating was performed at the Ångström Laboratory, Uppsala, Sweden. Calibration and age-depth modelling (Fig. 2) were conducted using Bacon (Blaauw and Christen, 2011), version 2.5, including the SHCal20 (Hogg et al., 2020) ^{14}C calibration curve. One sample, which contained modern carbon (pMC) was calibrated using the CALIBomb software (Reimer and Reimer, 2022: calib.org/calibomb)

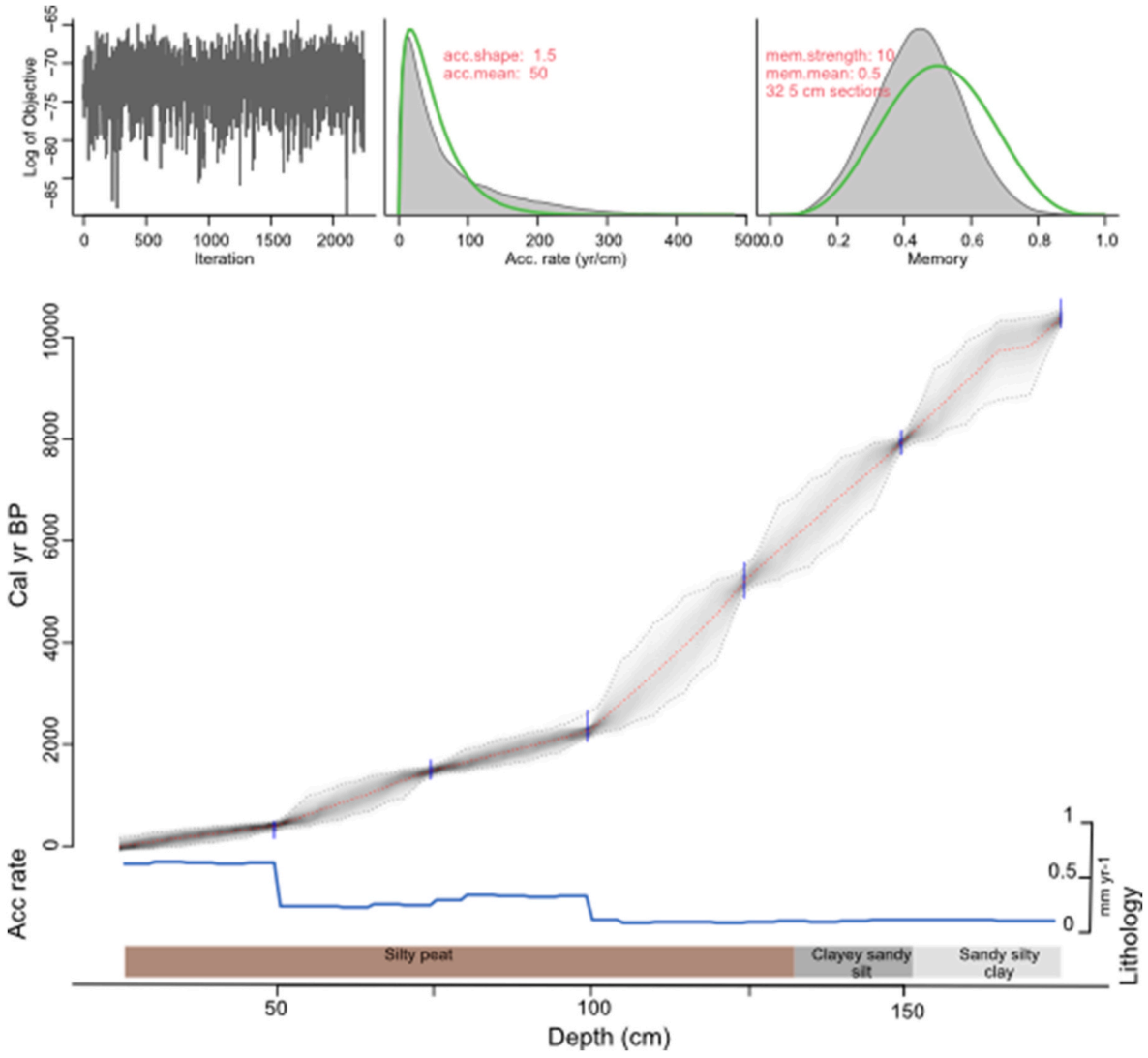

Fig. 2. Age-depth model for Marais Geluk sequence (25–175 cm). Calibrated probability distributions (Hogg et al., 2020) of the six ^{14}C dates are shown in blue. The weighted mean is represented by the red dotted line, and the grey shading indicates the 95% confidence range. The three top boxes show information about the model, from the left: quality of the iteration; predicted (grey shape) versus actual mean (green line), and values used in the a priori information used in the Bayesian approach (Blaauw and Christen, 2011). The blue line depicts the accumulation rate (mm yr^{-1}) throughout the sequence, followed by a general lithology description.

2.3. $\delta^{13}C$, TOC and TN analysis

Prior to analysis, samples were homogenized, freeze dried, weighed into silver capsules and treated with HCl to remove potential carbonates, meaning that the measurements were conducted on decarbonated samples. The TOC, TN and $\delta^{13}C$ analysis was conducted on a Flash-EA 1112 Elemental Analyzer (ThermoFisher Scientific) coupled to an isotope ratio mass spectrometer (IRMS, Delta V, ThermoFisher Scientific) at the Geological Institute, ETH Zurich. TOC and TN contents are reported in percent (%) of dry weight. For TOC, TN and $\delta^{13}C$, calibration was done using precisely weighed amounts of atropin ($\delta^{13}C = -21.4‰$) and peptone ($\delta^{13}C = -15.6‰$) standards. The reproducibility of the $\delta^{13}C$ measurements was better than 0.2‰.

2.4. CS-XRF and statistical processing

Prior to sub-sampling, the cores were scanned at the Department of Geological Sciences, Stockholm University, using an ITRAX XRF Core Scanner from Cox Analytical Systems. Analyses were made using a Mo tube set at 30 kV and 50 mA with a step size of 3 mm and a dwell time of 20s. Based on analytical performance (counting statistics above background), the following elements were selected for further processing and interpretation: Si, K, Ca, Ti, Mn, Fe, Ga, Rb, Sr, Y. In order to avoid matrix effects, a known pitfall where OM or water content dilute the signal, the data was normalized using a centered log-ratio (clr) transformation (Weltje et al., 2015). Outliers and zero values were removed prior to normalisation. Statistical associations were then assessed through PCA using the JMP 17 software, applying varimax rotation.

2.5. FTIR-ATR analysis and statistical processing

Eighty-six samples from the Marais Geluk sequence were analyzed for spectroscopic properties. Measurements were done on finely milled bulk samples by FTIR-ATR, in the mid-infrared range (4000-400 cm^{-1}), using a Cary-630 Agilent Technology spectrometer. The number of scans per sample was set to 200, recorded at 4 cm^{-1} resolution, with background measurements conducted before each measurement. Spectral processing (i.e., standardization, average and standard deviation spectra, as well as second derivative spectra) was done with the *{andurinha}* R package (Álvarez Fernández and Martínez Cortizas, 2020).

PCA was applied to the IR data on whole spectra using a transposed data matrix (i.e., samples in columns and wave numbers in rows). The PCA was performed with varimax rotation and in correlation mode. In multiphase samples, like bulk peat or lake sediments, many compounds (organic and inorganic) may overlap and thus be difficult to identify. As shown in previous studies, this may be overcome by decomposing the spectrum of each sample into several scores' spectra (Martínez Cortizas et al., 2021a, 2021b). In this way, peaks belonging to a particular compound will end up in their own component, which can be compared to reference spectra. The scores' spectra enable the main constituents/compounds present in the sample to be identified by interpreting their characteristic absorbances and comparing with spectra of reference materials (e.g., organic compounds and minerals). The square of the loading (i.e., partial communality) of a component in each sample accounts for the proportion of the spectral variance of the corresponding constituent/compound in the sample. The records of partial communalities reflect the changes in the relative abundance of the constituents/compounds along the sequence (depth or time variations) (Kylander et al., 2023; Martínez Cortizas et al., 2021b).

2.6. Pyrolysis GC-MS and statistical processing

Before the analyses, the samples were subjected to mild (single 2% HF) acid pretreatment to eliminate reactive minerals that may interfere with pyrolytic breakdown pathways of the OM (Kaal et al., 2019), modified after (Zegouagh et al., 2004). Nine of the 86 samples did not produce high-quality pyrograms due to insufficient sample amounts after HF treatment. Pyrolysis-GC-MS was performed with a Pyroprobe 5000 (CDS Analytical) coupled to a 5977 GC-MSD device from Agilent Technologies. Samples were embedded in glass wool-containing fire--polished quartz tubes. The samples were pyrolyzed at 650 °C (set-point temperature) for 10 s (heating rate 10°C ms^{-1}). Compounds were identified using available literature and previous analyses under the same conditions. Relative proportions of the compounds were calculated as the percentage of the total quantified peak area (TQPA), using the main ion fragments (m/z) of each product. In this paper we only consider organic compounds that may originate from pyrogenic OM such as benzene, benzonitrile and polycyclic aromatic hydrocarbons (PAHs) (Kaal et al., 2009), as indicators of fires in and around the Marais Geluk catchment.

As for the other datasets, pyrolysis data was summarized by PCA. In this case, the PCA was done on the direct matrix (pyrolysis products in columns and samples in rows), in correlation mode applying varimax rotation. Data was log-transformed before analysis.

2.7. Laser diffraction grain size analysis

Grain size analysis of the minerogenic particles in sediments and organic accumulations (e.g. peat) can yield a wealth of information on the depositional environment, transport processes and distances (e.g. Tsoar and Pye, 1987; Vandenberghe, 2013; Boggs, 2014). Grain size measurements were conducted through laser diffraction in a Malvern Mastersizer 3000 that was equipped with either a Hydro LV (600 mL volume) or a Hydro MV (120 mL volume), depending on sample size. The analysis was conducted at the Department of Geological Sciences, Stockholm University. The instrument employs a He-Ne red laser (λ = 632.8 nm) as well as a blue light LED (λ = 470 nm) with a 300 mm lens. Fresh material was collected at 19 depths throughout the sequence, from which the lithic fraction was isolated to minimize organic particle impacts on grain size parameters (e.g. Gray et al., 2010). This was done through soaking the samples in 17% H_2O_2 overnight and subsequently heating them over a 100 °C water bath until no visible organic particles remained. The samples were then diluted with deionized water and centrifuged for 10 min at 4000 rpm, after which the supernatant was removed. This process was repeated three times (following Sjöström et al., 2019). To facilitate particle disaggregation, sodium hexametaphosphate at a concentration 0.6% was added to the dispersion unit and the solution left for 3 min, followed by 60 s ultrasound treatment. The grain size distribution was measured for 60 s (30 s red light and 30 s blue light), with 5 repetitions, capturing grain sizes in 100 size classes from 0.01 μm (clay) to 3500 μm (coarse sand). Grain size classes are here described according to (Friedman and Sanders, 1978), and presented in three main size classes (clay: 0–2 μm; silt: 2–63 μm; and sand: 63–2000 μm).

2.8. pXRD mineral analysis

Powdered X-ray diffraction (pXRD) analysis reveal the mineral composition of the crystalline phases of sediments (Moore and Reynolds, 1997; Moreno et al., 2007; Sjöström et al., 2019). The pXRD analysis was conducted on HCl washed (10%) and milled ash residues, following (Sjöström et al., 2019). The analyses were conducted at the Swedish Museum of Natural History, Stockholm, using a PANalytical X–ray diffraction system (X'Pert^3 Powder) equipped with a multi detector. The samples were analyzed from 5° to 70° 2θ, with CuKα radiation (λ = 1.5406 Å) at 45 kV and 40 mA, passing through a curved graphite monochromator, fixed divergence and receiving slits (1°), step size 0.017° and a count time of 38 s. Processing of the diffractograms, such as determination of background, smoothing, peak localization and mineral identification was done in HighScore 4.6, a PANalytical software (Degen et al., 2014) with integrated mineral reference patterns from the ICSD

Table 1
Phytolith morpho-type and grass family assignment. The classification follows Twiss et al., (1969) and Twiss (1992), with adaptions based on references mentioned below.

GSSC morphotypes	Abbreviations and morphological description	Taxonomic group	Reference
Bilobate	**BIL-1:** elongated castula longer than width of lobes. Rounded, concave or plateaued lobes **BIL-2:** castula shorter than width of lobes. Rounded, concave, or truncated lobes **BIL-3:** typical Panicoid bilobate **BIL-4:** elongated Panicoid bilobate	Panicoideae, Aristidoideae	(Barboni and Bremond, 2009; Cordova, 2013, 2023; Finné et al., 2010)
Bilobate	**BIL-5:** trapezoidal, wide lobes	Danthonioideae, Pooideae	(Cordova, 2023; Finné et al., 2010; Fredlund and Tieszen, 1994)
Crenate	**CRE-1:** keeled **CRE-2:** elongate morphology, crenate OPS	Pooideae, Danthonioideae	(Cordova, 2023; Novello et al., 2018)
Cross	**CRO-1:** four lobes **CRO-2:** three lobes **CRO-3:** rounded	Panicoideae	(Barboni and Bremond, 2009; Cordova, 2023; Rossouw, 2009)
Polylobate	**POL-1:** three defined lobes along castula	Panicoideae	
Rondel	**RON-1:** conical **RON-2:** oblong **RON-3:** round-base **RON-4:** reniform **RON-5:** rectangular **RON-6:** circular	Pooideae, Danthonioideae, Ehrhartoideae, Arundinoideae	(Cordova, 2013, 2023; Neumann et al., 2019; Rossouw, 2009; Sjöström et al., 2019)
Saddle	**SAD-1:** symmetrical **SAD-2:** concave **SAD-3:** rounded	Chloridoideae, Aristidoideae	(Barboni and Bremond, 2009; Breman, 2010; Cordova, 2023; Finné et al., 2010; Rossouw, 2009)
Trapezoid	**TRZ-1:** elongated trapeziform **TRZ-2:** polygonal	Pooideae	(Finné et al., 2010; Rossouw, 2009)
Non-Poaceae	Papillae and cone	Cyperaceae	(Alexandre et al., 1997; Finné et al., 2010)
Non-diagnostic	**SPH-PSI:** spheroid psilate **NON-2:** polygonal **NON-3:** trigonal pyramid psilate		(Lisztes-Szabó et al., 2014; Novello et al., 2012, 2018)

database (2012). Brindley and Brown (1984) and Moore and Reynolds (1997) were also used to guide mineral identification.

2.9. GSSC phytolith analysis

Since GSSC phytolith analysis is more laborious compared to isotope analysis, we took the approach of analyzing selected samples (n = 14) throughout the sequence and using the phytolith results as an aid when interpreting the $\delta^{13}C$ results. Sample preparation for phytolith analysis followed the standard laboratory method of Battarbee (1986) for the recovery of siliceous microfossils, which will recover both phytoliths and diatoms. Circa 1g of sample was retrieved from the fresh sediment, soaked with 17% H_2O_2, left at room temperature overnight, and thereafter heated to reaction temperature (80°C) in a water bath and left to react for at least 2 h. Clay particles were removed by repeatedly decanting at 2-h intervals. To disaggregate any adhered clay particles, diluted NH_3 was also added during the decanting process. Finally, samples were mounted onto microscope slides using Naphrax resin (Finné et al., 2010).

Phytoliths were identified under a light microscope at 1000× magnification (Finné et al., 2010). Total diatom occurrence was also noted, without any attempt to identify species or genera. A minimum of 250 GSSCs were counted per sample to ensure a representative GSSC phytolith assemblage (Twiss, 1992). Naming of the phytolith morpho-types followed the ICPN-2.0 nomenclature (Neumann et al., 2019). A number of diagnostic GSSC groups for the Panicoideae (mostly C_4), Pooideae (C_3), Ehrartoideae (C_3), Danthoniodeae (C_3) and Chloridoideae (C_4) subfamilies were identified using the standard GSSC classification scheme of Twiss et al. (1969), with adaptations of this scheme to a South African palaeoecological context, as outlined in Table 1. Based on this classification scheme, phytolith GSSC morpho-types were assigned to different grass families - C_3 or C_4 grasses - or to the indeterminate category.

To depict relative changes two phytolith ratios were explored. The two ratios are based on the original *Ic*-index (Twiss et al., 1969) and *Iph*-index ((Alexandre et al., 1997; Diester-Haas et al., 1973), respectively, adapted to a South African context following Cordova (2023). The first index, which depicts relative changes between C_3 and C_4 grasses is calculated by dividing the sum of GSSC morphotypes related to C_3 sub-families (Pooideae, Danthoniodeae, Ehrhartoideae) against the total sum of diagnostic GSSC phytoliths:

$$C3 / C4 = \frac{Pooid. + Danth. + Ehrhar.}{\text{Pooid.} + \text{Danth.} + \text{Ehrhar.} + \text{Panicoi.} + \text{Chlori.}}. \quad (1)$$

The second ratio, the Panicoideae index (Cordova, 2023), depicts relative moisture changes, particularly summer precipitation, by comparing moisture adapted C_4-Panicoideae against all C_4 grass morpho-types (C_4-Chloridoideae and C_4-Panicoideae), calculated as follows:

$$Panicoideae\ index = \frac{Panicoi..}{Chloridoi. + Panicoi.} \quad (2)$$

3. Results

3.1. Radiocarbon ages, age-depth modelling and lithology

The lowermost sample provided a calibrated age of 10,380 cal yr BP (weighted mean, rounded to nearest decade) (Fig. 2). The results show that all dates are in chronological order (Table 2), and that the accumulation rates were significantly lower in the early part of the record (175–102 cm, average: 0.09 mm yr^{-1}) compared to the uppermost part (>102 cm, average: 0.7 mm yr^{-1}). Modern carbon (pMC) was present in the uppermost dated sample (25-cm depth), indicating that it originates from a post-bomb age (Reimer et al., 2004). Post-bomb calibration (CALIBomb software) showed that this sample had an age of either 1957 CE or 2009–2013 CE (Table 2). This post-bomb date, at 25-cm depth, indicates the uppermost part of the sequence is disturbed, potentially from grazing animals, and the focus will therefore be on results below 25 cm. All results presented below are presented in relation to calibrated years before present (cal yr BP).

Table 2
Depth, sample-id, radiocarbon and calibrated ages.

Depth (cm)	Lab-id	14C yr ±1σ	Calibrated Age Range, BP or CE. 2σ
25	Ua-73695	105.4 ± 0.3 *pMC*	1957 CE, *(2009–*2013 CE*)*
50	Ua-73696	335 ± 28	448–299
75	Ua-73697	1646 ± 29	1562–1412
100	Ua-73698	2298 ± 29	2342–2144
125	Ua-73699	4599 ± 31	5440–5050
150	Ua-73700	7155 ± 34	8015–7860
175	Ua-73701	9284 ± 40	10560–10260

The lowermost 25 cm of the sequence (10,380–7900 cal yr BP), consisted of a minerogenic clayey silt, followed by a darker peaty silty unit between 150 and 132 cm (7900–5900 cal yr BP). From 132 to 25 cm (5900–0 cal yr BP) a dark silty, peaty unit occurred (Fig. 2). Information on the main color variability through the sequence can be found in the Supplementary data.

3.2. LOI, TOC, TN, and $\delta^{13}C$

The results show that the loss following ignition at 550°C ranged from 7 to 37% through the sequence (average: 21.5 ± 17%, n = 73, all standard deviations are here given as 2σ, Fig. 3). Between 10,380 and 7640 cal yr BP, lower values (<10%, n = 14) occur (Fig. 3), followed by a gradual increase towards 5270 cal yr BP (n = 11). Higher values (27 ± 3.8%, n = 48) are thereafter recorded until 180 cal yr BP. Peaks are noted at 3700, 3070, 2080, 1900–1400, 900 and 580 cal yr BP. Between 410 and 180 cal yr BP oscillations between higher and lower values are observed.

The TOC and TN content (TOC average: 10 ± 10%; TN average: 0.5 ± 0.5%, n = 73) generally follow the same pattern as the LOI, with overall low, but gradually increasing, values in the oldest part of the sequence (TOC average: 2.6 ± 0.9%; TN average: 0.13 ± 0.01%, n = 14). This increase accelerates between 7530 and 5380 cal yr BP (Fig. 3). From 5000 cal yr BP, high, but variable, values occur (TOC average: 13 ± 6%; TN average: 0.7 ± 0.2%, n = 46), followed by decreasing content. The C/N (molar) ratio varies between 16 and 32 (average: 24 ± 9, n =

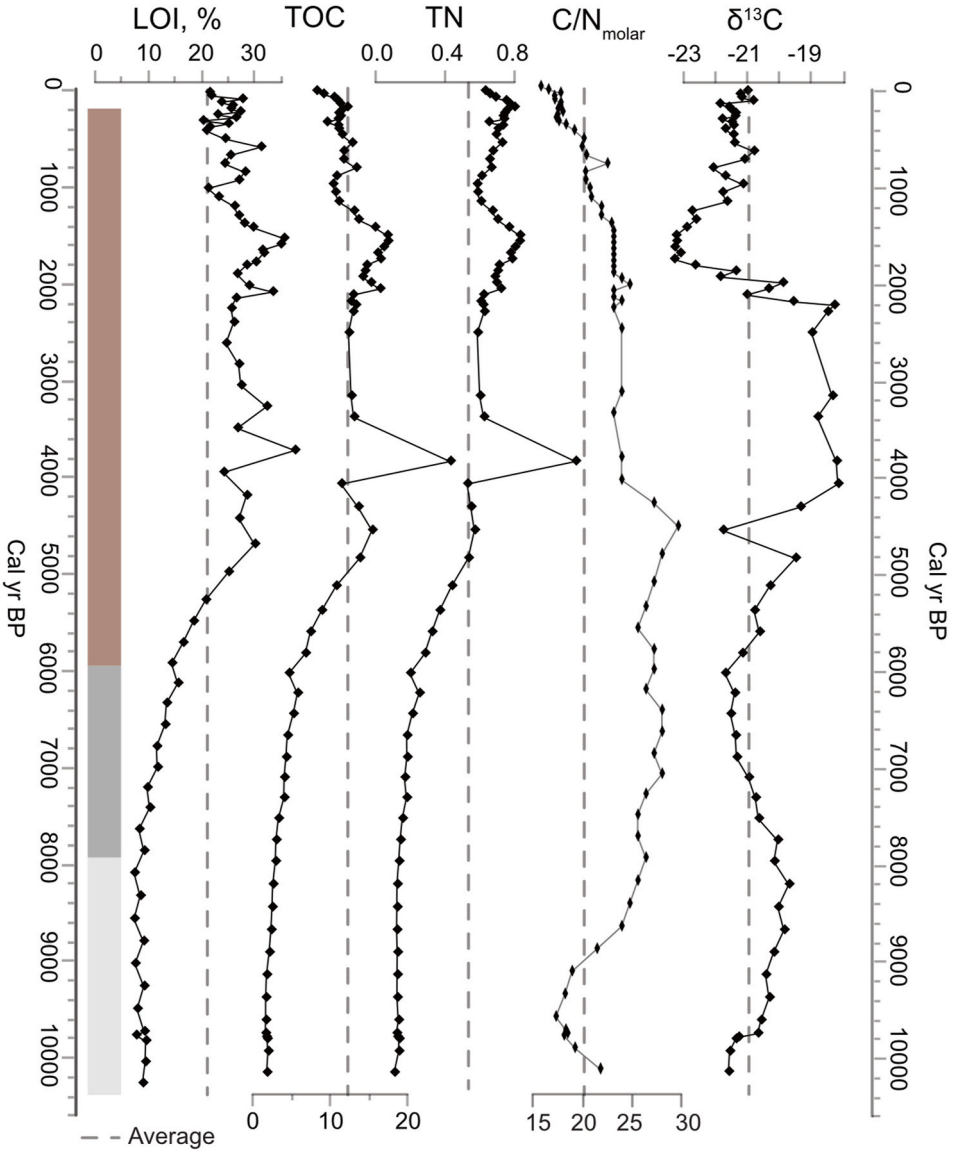

Fig. 3. LOI, TOC, TN, C/N ratio and $\delta^{13}C_{bulk}$ plotted against time.

73) through the sequence. Decreasing values are noted early in the sequence (10,260–9810 cal yr BP, n = 3), with average values of 19 ± 3.8, n = 6) sustained until 9140 cal yr BP, when values increase again. Between 8680 and 4450 cal yr BP values stay elevated (n = 19), followed by a steep decrease. Lower, but stable, values are noted thereafter until 2280 cal yr BP, followed by generally declining values towards the present. C/N ratios below 20 are again observed from 400 cal yr BP towards the present. The $\delta^{13}C$ values range from −23 to −18‰ (average: −21 ± 2.9‰, n = 73) with overall less variability between 10,150 and 5120 cal yr BP (min: −21‰, max: −20‰), compared to after 5100 cal yr BP. Between 4310 and 2180 cal yr BP, enriched (18.7 ± 1.0‰, n = 9) values were observed. Thereafter, a rapid, but stepwise decrease occurs. The lowest values throughout the record are observed between 1810 and 1240 cal yr BP (−23 ± 0.5‰, n = 8), followed by a stepwise increase towards the present.

Table 3
Statistical association of elemental downcore, variation. Strongly associated variables (±>0.7, **bold**), moderately associated variables (±0.3–0.69, normal), and weak association (−0.3 – 0.3, grey).

Variables	XRFCp1	XRFCp2	XRFCp3
Var %	0.44	0.21	0.19
Cum. var. %	0.44	0.64	0.84
Si	**0.79**	−0.48	−0.04
K	**0.78**	−0.57	0.02
Rb	**0.78**	−0.12	0.30
Ti	**0.77**	−0.54	−0.22
Mn	−0.06	**0.98**	−0.06
Sr	−0.10	−0.36	**0.79**
Ca	−0.67	−0.02	0.61
Y	**−0.79**	−0.19	0.24
Ga	**−0.90**	−0.01	−0.05
Fe	−0.19	−0.30	**−0.86**

3.3. CS-XRF results and statistical associations

Relative concentrations of elements Si, K, Ti, Rb, Mn, Sr, Ca, Y, Ga and Fe (clr-transformed) are here used to infer downcore variations between 25 and 174 cm. The variability of individual elemental profiles is depicted in Fig. 4.

Principal component analysis showed that three components capture 84% of the variability (Table 3). The first component (XRFCp1) accounted for 44% of the variance, with elements Si, K, Rb and Ti strongly (>0.7) associated, while Y and Ga were strongly negatively (<-0.7) associated. A negative association to XRFCp1 is also observed for Ca (−0.67). XRFCp2 (21% of the variance) showed a very strong positive association (>0.98) of Mn and a moderate negative association of Si, K, Ti and Sr. XRFCp3 (19% of the total variance), has a strong association with Sr (positive) and Fe (negative), and a moderate association with Ca. By plotting downcore variability of the component scores, temporal variability can be assessed (Fig. 5). In the lowermost, and oldest, part of the sequence (10,300–9160 cal yr BP) scores on XRFCp1 displayed variable, but generally increasing values. Sustained elevated values thereafter occurred until 6560 cal yr BP. Between 6540 and 6060 cal yr BP, the values were generally lower, followed by less variability and mostly positive scores until 3930 cal yr BP. After 3570 cal yr BP, towards the present, mostly negative scores were observed, with positive (>0.1) values noted at: 3530, 3420, 3000, 2810–2310, 2060, 1980, 1130–1055,

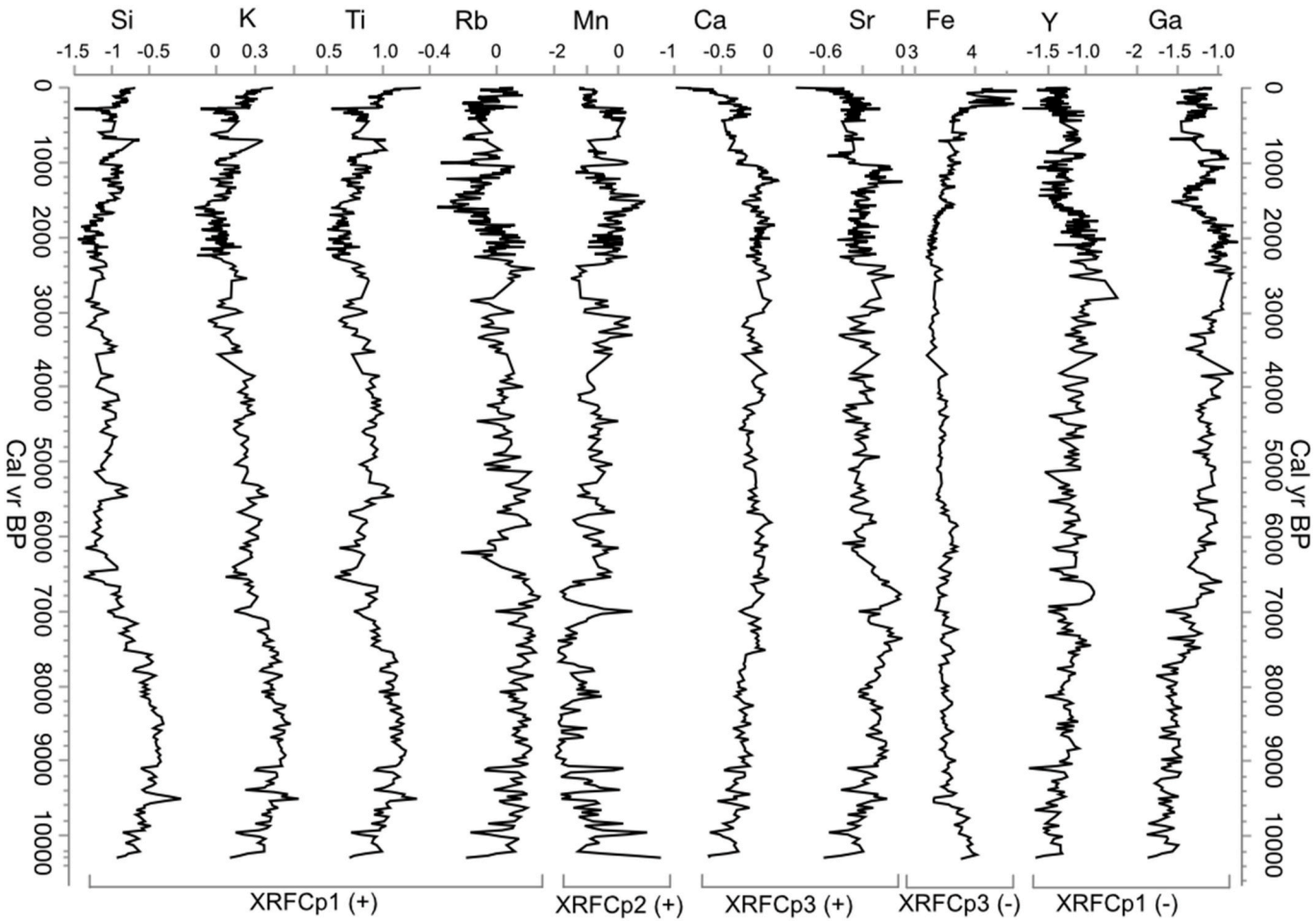

Fig. 4. Results of CS-XRF analysis (clr transformed data) and major statistical associations.

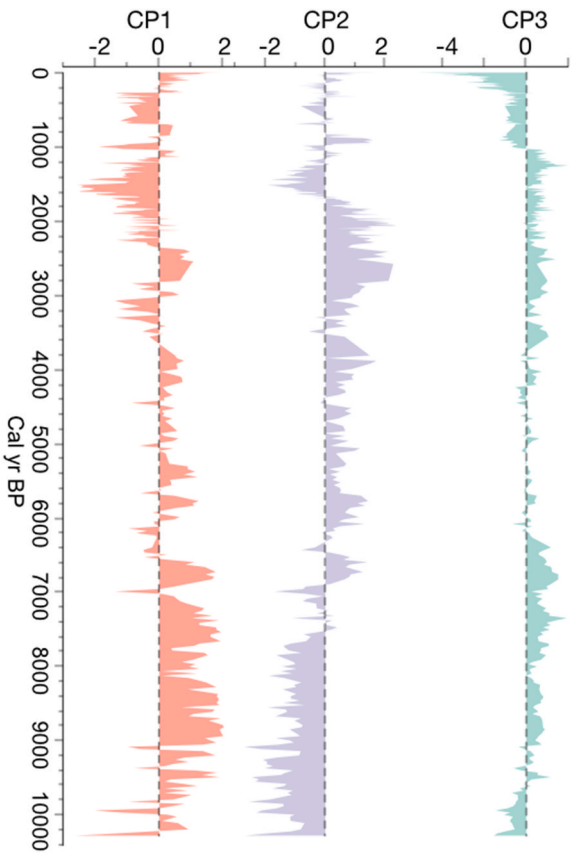

Fig. 5. Weight of the rotated components (1–3) over time. Average indicated by grey, dotted, line.

910, 850–700, 260–225 and 180–0 cal yr BP.

Component 2 (XRFCp2) displays negative scores between 10,300 and 7550 cal yr BP. This interval is followed by a few, short duration, episodes of positive values (7490; 7,00; 7330 and 7260 cal yr BP). Negative values are observed again between 7230 and 6940 cal yr BP, followed by positives scores until 6470 cal yr BP. Between 6440 and 6120 cal yr BP oscillations between negative and positive values occurred, followed by a longer period of mostly positive scores between 6100 and 1700 cal yr BP, with drops observed at 4400 and 3310 cal yr BP. Lower values were observed again between 1679 and 330 cal yr BP, followed by oscillating values towards the present.

Component 3 (XRFCp3) shows negative scores from 10,300 until 9660 cal yr BP, followed by mostly positive values until 6220 cal yr BP. Thereafter the values stay around zero until 4500 cal yr BP. Lower values occur between 4460 and 4210 cal yr BP, followed by three periods of positive scores (4180–3930; 3850 and 3560–3380 cal yr BP). Between 3270 and 1030 cal yr BP, positive scores are observed, followed by negative values towards the present.

3.4. FTIR-ATR

The spectra of the samples, the standard deviation spectrum and the average second derivative spectrum are depicted in Fig. 6. The largest absorbances were found in the 1200-900 cm^{-1} and the 500-400 cm^{-1} regions, with moderate absorbances between 900 and 600 cm^{-1}. Low but detectable absorbances were also found in the 3700-2800 cm^{-1} and in the 1800-1300 cm^{-1} regions (Fig. 6, upper panel).

The second derivative (Fig. 6, bottom panel) identified absorbances that correspond to two main inorganic constituents: silicic clays (3698, 3653, 3623, 1001, 937, 909, 865, 632 and 606 cm^{-1}), and quartz (1165, 1141, 1109, 1083, 1060, 1031, 798, 777, 693, 527, and 464 cm^{-1}) (Müller et al., 2014; Tinti et al., 2015). Other silicates, as albite (1096, 1031, 980, 882, 751, 693, 649, 587, 527, 464, and 421 cm^{-1}), and mica (1165, 1141, 1109, 1083, 1031, 980, 751, 649, 606, 587, 527, 464, 449, and 421 cm^{-1}), as well as biogenic silica (1236, 1096, 1031, 1060, 962, 937, and 751 cm^{-1}), may also be present but they are difficult to assess as most of their main absorbances overlap or coincide with those of quartz and clays. The second derivative spectra (Fig. 6, bottom panel) also enabled organic compounds to be identified as vibrations from aliphatic functionalities (2920 and 2850 cm^{-1}). The second derivative is not efficient in identifying the location of broad peaks and thus the 1800–1200 region is almost flat in this spectrum. But the absorbance spectra (Fig. 6, upper panel) show small variations in the 1700-1600 cm^{-1} region, that can correspond to carboxylic, aromatic and nitrogenated compounds, and in the 1500-1300 cm^{-1} region, usually assigned to aromatic and aliphatic OM.

The standard deviation spectrum (Fig. 6, mid panel) shows that the largest variability (i.e., largest differences between samples) occurs in the 1100-900 cm^{-1} region (mainly silicates' absorbances) and at ~527 cm^{-1}, which also corresponds to silicates (silicate clays and albite). Moderate variability is shown in peaks characteristic of clays (3700-3600 cm^{-1} region), quartz (the 798 and 777 cm^{-1} doublet), and in the 1300-1200 cm^{-1} region (which may correspond to biogenic silica); and lower variability in absorbances related to organic compounds (2920, 2850, 1700-1300 cm^{-1}).

As indicated in the methods sections, to help with the identification of sample constituents we performed a PCA on the transposed IR matrix. We forced the PCA to extract ten components to ensure that at least 99% of the total IR spectral variance of each sample was accounted for the extracted components. Based on the consistency of the depth records of the partial communalities, which are an indication of the relative variation of the sample constituents, we selected five components (IRCp1 to IRCp4, and IRCp9) for further description and discussion. The scores spectra and the records of partial communalities are found in Figs. 7 and 8.

The spectrum of IRCp1 scores (Fig. 7) is dominated by absorbances of silicate clays and other silicate primary minerals (Müller et al., 2014). Absorbances at 3698, 3651, 3621, 1023, 936, 909, 684, and 522 cm^{-1} can be associated to clays (i.e., kaolinite), while absorbances at 993, 978, 876, and 742 may correspond to both albite and mica. The record of IRCp1 loadings (Fig. 8) shows the largest values (0.81–0.83; partial communalities of 63–69% of the MIR spectral variance (MIRsv) in samples older than 8910 cal yr BP, indicating a predominance of clay particles in the sediments. Values decrease slightly by 8680 cal yr BP and remain with relatively low variability (53–62% MIRsv) until ca. 5820 cal yr BP when values decrease again (to 50% MIRsv) until ca. 4550 cal yr BP. From this date until ca. 1930 cal yr BP values remain almost constant (50–52% MIR spectral signal). Clay contribution to the IR signal decreases between ca. 1870 and ca. 1250 cal yr BP, to reach a local minimum (42% MIRsv) by ca. 1500 cal yr BP. Values thereafter return to those of the previous phase.

The spectrum of IRCp2 scores (Fig. 7) shows the characteristic features of biogenic silica (bSi; Gendron-Badou et al., 2003; Swann and Patwardhan, 2011; Meyer-Jacob et al., 2014), with absorbances between 1000 and 1200 cm^{-1}, peaking around 1100 cm^{-1}, and at 800 and 470 cm^{-1}. Low but detectable absorbances of OM compounds are also observed at 2917 and 2850 cm^{-1} typical of aliphatic moieties, and at 1600-1650 cm^{-1} due to vibrations characteristic of nitrogenated (i.e., proteins) and aromatic compounds. Partial communalities vary between a minimum of 30% and a maximum of 75% of the MIRsv, showing the same periods but opposite distribution to the clay (Fig. 8). Thus, clay and bSi are the main components of the sediment sequence detected by IR, accounting for >99% of the MIRsv.

IRCp3 score's spectrum corresponds to that of quartz, with typical absorbances at 1665, 1139, 1087, 1059, 798, 777, 693, and 451 cm^{-1} (Fig. 7). Partial communalities are very low (<0.1%) and homogeneous for samples older than ca. 9150 cal yr BP (Fig. 8). The largest values (i.e.,

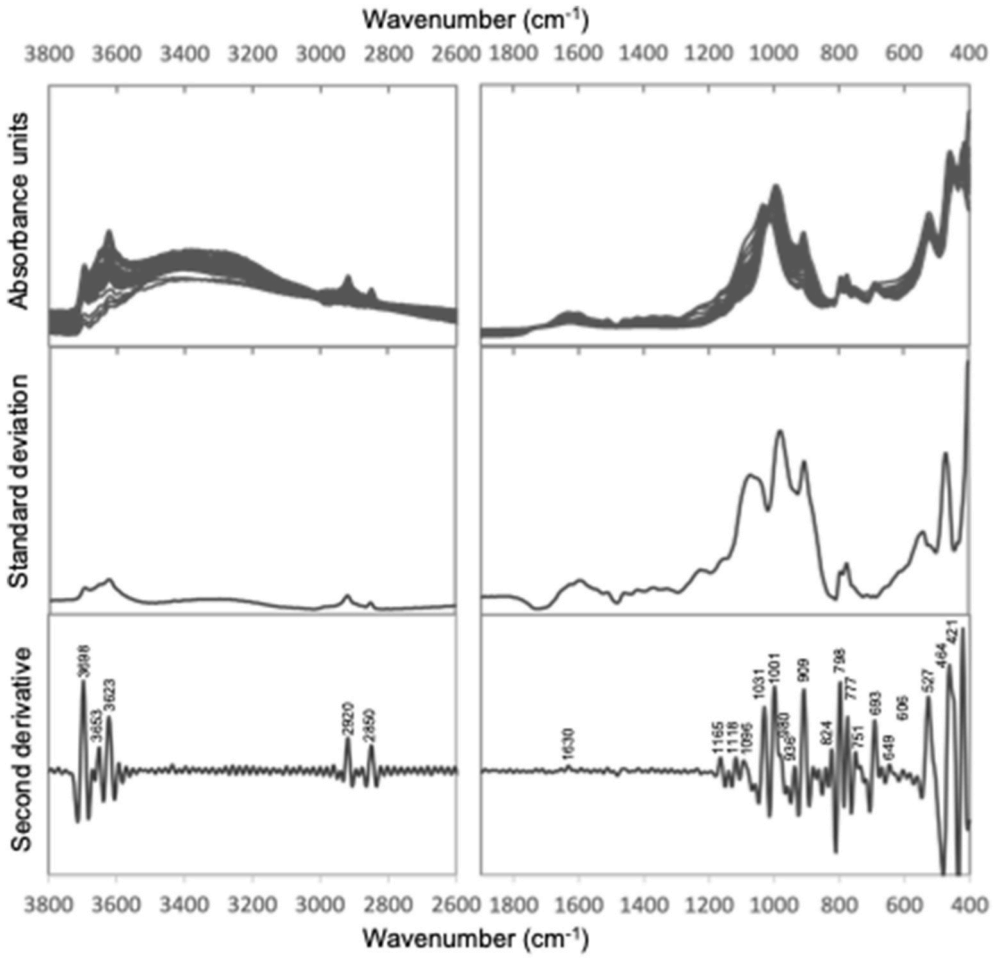

Fig. 6. Absorbance spectra, standard deviation spectrum and average second derivative spectrum of the Marais Geluk sequence samples. Note that the second derivative spectrum has been reversed to match with peaks in the absorbance spectra.

quartz contribution to MIRsv, >0.3%) are reached between ca. 8910 and ca. 6450 cal yr BP. Overall low values occur between ca. 6230 and ca. 4305 cal yr BP, with two local minima at ca. 5800 and ca. 4830 cal yr BP, followed by slightly higher values until ca. 2110 cal yr BP. Values decrease and remain low until 1150 cal yr BP, with a minimum between ca. 1680 and 1500 cal yr BP, resuming after ca. 1330 cal yr BP to values similar of the previous phase.

Absorbances of organic compounds dominate the IRCp4 record of scores: 2919 and 2850 cm^{-1} (aliphatic moieties), 1586 cm^{-1} (nitrogenated compounds), 1465 and 1264 cm^{-1} (lignin), 1031 cm^{-1} (carbohydrates) (Fig. 7). The spectrum also contains absorbances corresponding to clay minerals (3698, 3651, 3621, 911, 693, 531 and 457 cm^{-1}). The record of partial communalities (Fig. 8) shows moderate values until ca. 8910 cal yr BP, followed by a decreasing trend and low variation until ca. 6900 cal yr BP. Values increase and remain high until ca. 1240 cal yr BP, showing three maxima by ca. 6030, 4550 and 1620 cal yr BP. After that, a stepwise decrease occurs.

The record of IRCp9 scores is complex but shows IR features similar to those of charcoal, with large relative signals of carboxylated and aromatic compounds (1500-1600 cm^{-1}) and aliphatic compounds (2800-2950 cm^{-1}) (Constantine et al., 2021; De la Rosa et al., 2019) (Fig. 7). Absorbances that can be associated to inorganic clays and quartz are also observed. These inorganic materials are known to be included in charcoal pores (Kaal et al., 2008). The chronology of partial communalities shows overall low values, with a slight increase around 5820 cal yr BP and the largest values observed between ca. 4070-2200 cal yr BP (Fig. 8).

Some of the selected IR components show significant correlations to the proxies for OM content (C, N and C/N), isotopic ($\delta^{13}C_{bulk}$) and elemental composition (CS-XRF) (Table 4). A full table, with Pearson correlation coefficients for all individual CS-XRF elements, can be found in the Supplementary information (S.Table 1). IRCp1 (negative) and IRCp2 (positive) strongly correlate with TOC and TN content (Table 6); they also show low to moderate correlation to $\delta^{13}C_{bulk}$ (positive and negative, respectively), while IRCp9 correlates (positive) with C/N and $\delta^{13}C_{bulk}$. IRCp1 is also positively correlated to XRFCp1 and negatively to XRFCp2. As expected, IRCp2 shows the opposite correlation pattern. IRCp4 (fresh OM) is negatively correlated to XRFCP1, while IRCp9 shows moderate correlation to C/N, XRFCp2 and XRFCp3.

3.5. *Pyrolysis GC-MS*

Pyrolysis analyses identified eight organic compounds that can be related to pyrogenic OM. These were one monocyclic aromatic (benzene), one nitrogenated compound (benzonitrile), and six polyaromatic hydrocarbons (PAHs: biphenyl, naphthalene, 1-methylnaphthalene, 2-methylnapthalene, C_2-alkylnaphthalene, and fluorene). The PCA extracted three components explaining 43% (PyCp1), 38% (PyCp2), and 12% (PyCp3) respectively of the total variance. PyCp3 only showed a high loading for benzene (Table 5), and because benzene has a weak proxy value for pyrogenic matter when present in uncharred organic matrix, PyCp3 is not further considered here. PyCp1 showed large loadings (0.84–0.92, Table 5) for benzonitrile, biphenyl, naphthalene, and fluorene; while PyCp2 showed large loadings (0.89–0.92, Table 5)

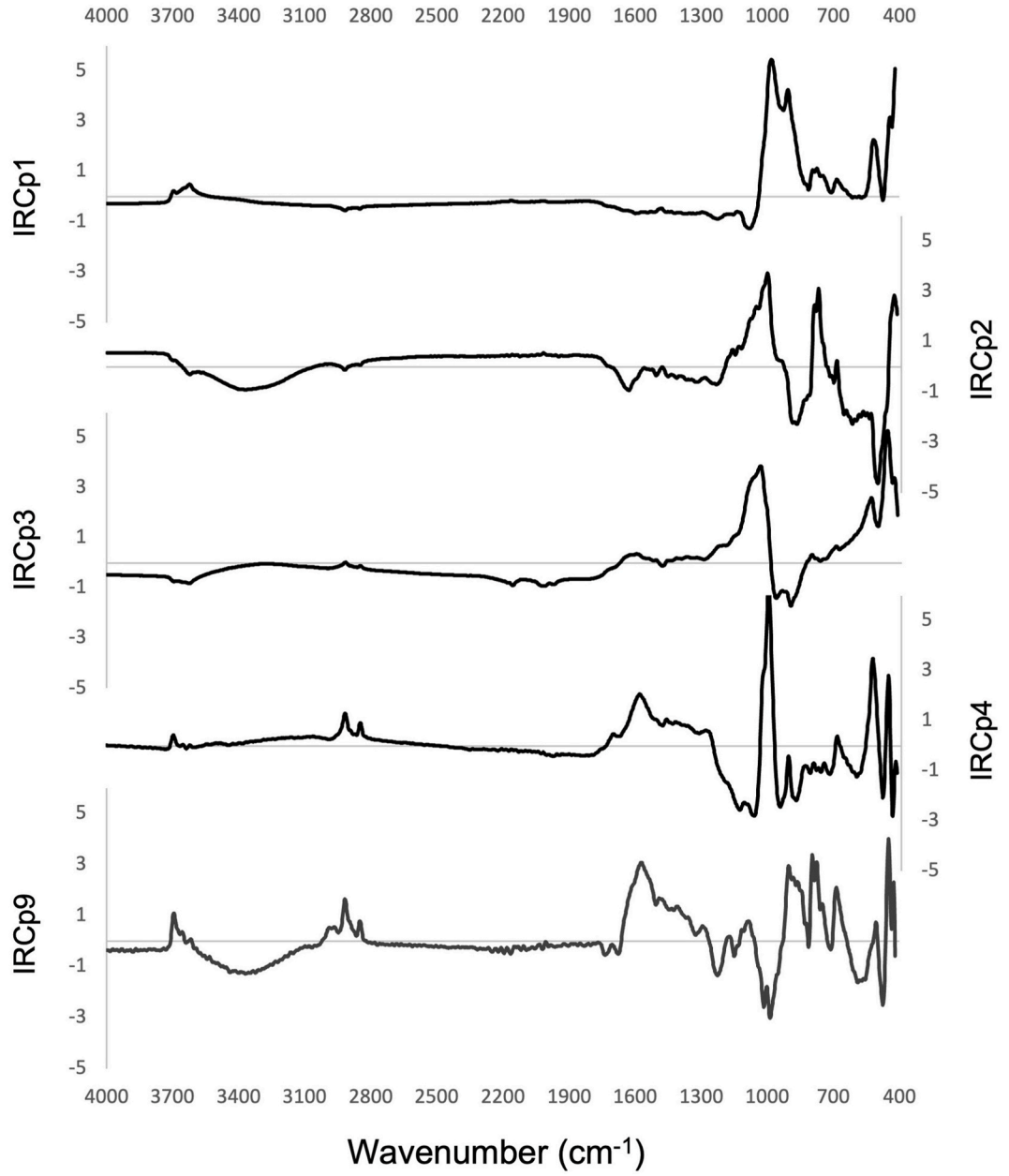

Fig. 7. Spectra of scores of the principal components extracted on the whole MIR transposed spectra (i.e., samples in columns and wavenumbers in rows).

for 1-methylnaphthalene, 2-methylnaphthalene and C_2-alkylnaphthalene). The compounds related to PyCp1 probably represent the most reliable signal of pyrogenic OM, as these unsubstituted PAHs are preferentially formed upon pyrolysis of strongly charred material, whereas the alkyl-substituted PAHs are associated with weakly charred material and even uncharred biomass constituents like resins and other volatiles (e.g. Kaal et al., 2009).

The chronology of the scores of both components (Fig. 9) shows quite similar variations, except for the period between ca. 5820 and 2180 cal yr BP. The overall trend is a decrease in scores from the base of the sequence to the surface, interrupted by two brief phases of increase centered around 1400 and 260 cal yr BP, respectively. Between 5820 and 2180 cal yr BP the pyrogenic OM proxies decoupled, with those associated to PyCp1 displaying a large increase while those associated to PyCp2 are relatively depleted. This corroborates the argument that Py Cp1 reflects pyrogenic OM whereas PyCp2 is likely associated with a non-pyrogenic source of OM.

3.6. Laser diffraction grain size analysis

The results of the grain size analysis showed that the majority of samples are dominated by silt sized particles (60–80%), polymodal frequency distribution and poor sorting (Table 6). Clay sized particles vary from 27 to 12% throughout the sequence, with the lowermost sample (9770 cal yr BP) containing the highest clay size concentration (27%) and finest mode (0.8 μm). This sample is also the most unsorted, and the only sample containing very coarse sand (0.1%). Between 9500 and 3490 cal yr BP (n = 8) the mode gradually decreases as a response to a gradual decrease of sand content (Table 6). Following the decrease, the mode and sand content increases again, with peaks at 1880 cal yr BP (mode: 32 μm). From 1370 cal yr BP towards the present, fine silt dominates (mode: 8–9), with one exception noted around 250 cal yr BP where sand content is elevated (11%, mode: 30 μm). The grain size is skewed towards finer particles throughout the sequence (>1, Blott and Pye, 2001) (Table 6).

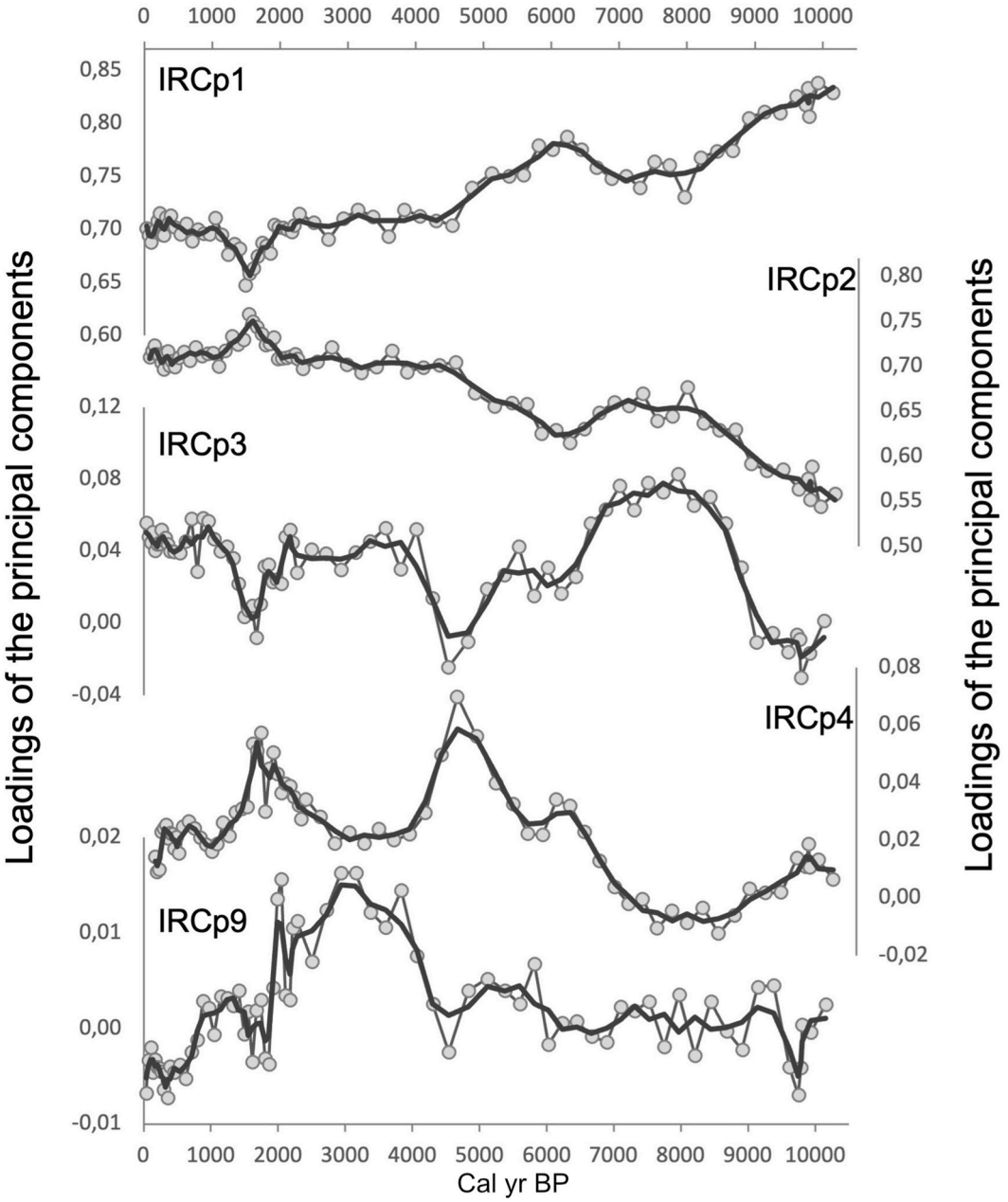

Fig. 8. Records of loadings of the six principal components selected from the PCA on the MIR data.

3.7. pXRD

The pXRD analysis showed that the mineral phases occurring throughout the sequence are quartz, alkali-feldspar, albite, clay, magnetite and anatase (S. Fig. 3). The relative distribution is dominated by quartz and clay minerals. The clay mineral phase occurs as two broad peaks, one between 12 and 10 Å and another around 4.50 Å. These peaks represent either a smectite and/or kaolinite clay mineral. Both smectite and kaolinite display peaks in these regions after heat treatment (as

Table 4
Pearson correlation coefficients for the correlation, between the extracted IR proxies for organic matter content and composition (TOC, TN, C/N, $\delta^{13}C_{bulk}$), and proxies for inorganic matter (CS-XRF components).

Variables	IRCp1	IRCp2	IRCp3	IRCp4	IRCp9
TOC	**−0.91**	**0.89**	−0.25	0.17	0.03
TN	**−0.93**	**0.92**	−0.16	0.08	−0.13
C/N	0.14	−0.14	0.09	0.18	0.47
$\delta^{13}C_{bulk}$	0.58	−0.54	0.28	−0.12	0.02
XRFCp1	0.55	−0.53	0.23	−0.61	−0.03
XRFCp2	−0.50	0.53	0.20	0.45	0.49
XRFCp3	0.03	−0.03	0.02	0.08	0.47

Table 5
Loadings of the principal components extracted by the PCA on the pyrolysis compounds related to pyrogenic organic matter.

Variables	PyCp1	PyCp2	PyCp3
benzene	0.49	0.35	**0.80**
benzonitrile	**0.84**	0.33	0.19
biphenyl	**0.92**	0.16	0.26
naphthalene	**0.86**	0.32	0.32
1-methylnaphthalene	0.33	**0.89**	0.21
2-methylnaphthalene	0.31	**0.93**	0.11
C2-alkylnaphthalene	0.19	**0.92**	0.22
fluorene	**0.85**	0.43	0.15

Table 6
Summary results of the laser grain size analysis. The grain size sorting was calculated using the Gradistat software (ver 9.1, geometric method of moments).

Age (cal. yr BP)	Depth (cm)	Dx10 (μm)	Dx50 (μm)	Dx90 (μm)	Clay% <2 μm	Silt% 2–63 μm	Sand% 63-2k μm	Mode (μm)	Sorting	Skewness
120	32	1	9	60	20	72	9	8	4.1	5.45
250	40	1	10	70	20	69	11	30	4.4	3.24
380	48	1	9	50	18	76	6	9	4.4	2.77
670	56	1	9	50	18	75	6	9	3.8	6.07
970	64	1	9	53	19	74	7	9	3.9	5.61
1370	72	1	9	56	18	74	8	9	3.9	4.71
1650	80	2	16	73	13	75	12	27	3.9	2.81
1900	88	1.5	16	99	16	67	18	32	4.6	2.24
2220	98	1	13	82	18	69	13	25	4.5	3.64
2613	103	1	12	75	18	71	11	19	4.4	4.22
3490	111	1.5	9	79	18	70	12	5	4.5	3.56
3950	115	1	9	51	20	74	6	8	3.9	3.65
4980	123	1	12	64	17	74	9	24	4.1	3.43
5490	127	2	16	141	13	66	21	19	4.9	2.81
6330	135	2	12	58	12	80	8	21	3.5	3.15
7200	143	1.5	12	73	17	71	11	27	4.3	3.57
8460	155	1.5	15	85	15	71	15	36	4.3	2.54
9500	163	1	18	89	18	66	16	46	4.9	2.22
9770	167	0.8	8	80	27	60	12	0.7	5.7	6.36

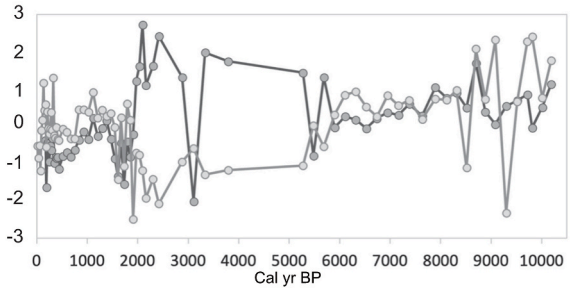

Fig. 9. Chronology of the PyCp1 (black) and PyCp2 (grey) scores of the pyrolysis compounds related to pyrogenic organic matter.

applied here, LOI, 550 °C) (Brindley and Brown, 1984). In addition, a broad amorphous reflection is noted between 20 and 30° 2θ, likely representing biogenic (amorphous) silica (Eisma and Van Der Gaast, 1971). The pXRD mineral results are generally in line with the findings from FTIR-ATR results (chapter 3.4).

3.8. GSSC phytolith analysis

Here, the result of the two phytolith indices, namely the C_3/C_4 and Panicoideae indices, are presented, while the full GSSC phytolith dataset is found in the supplementary material (S. Fig. 2). Overall, the phytolith assemblage is dominated by morpho-types related to C_3 grasses. This likely reflects that locally, near the wetland borders, C_3 grasses may occur in greater occurrence compared to the surrounding grassland. This pattern was also observed at the nearby Braamhoek wetland (Finné et al., 2010; Norström et al., 2014). Between 10,260 and 8090 the C_3/C_4 index decreases, followed by elevated values until 2400 cal yr BP, after which the index decreases again towards the present. Between 10,300 and 5920 cal yr BP the Panicoideae Index stays around 50%, except for a decline in value at 8090 cal yr BP (38%, increase in C_4-Chloridoideae). After 8090 cal yr BP, the Panicoideae Index generally increases reaching maximum values at 3050 cal yr BP (79%). In the following samples, somewhat higher Panicoideae values are observed, varying between 52 and 76%. Diatoms were only observed in four samples: 4700 (n = 8), 2400 (n = 2), 1650 (n=10); 840 (n = 9) and 250 cal yr BP (n = 277).

4. Discussion

4.1. Wetland development

Here, the general properties of the Marais Geluk sequence are explored. To facilitate the discussion and multi-proxy interpretation, the sequence is divided into two units: Unit I and Unit II, each with two subunits (a and b, see Fig. 10). The local wetland development is inferred from organic content (LOI, TOC), together with the vegetation proxies ($\delta^{13}C_{bulk}$, GSSC phytoliths and C/N) and sedimentology (lithology, grain size). The $\delta^{13}C_{bulk}$ is used to infer changes in the local wetland vegetation, while the GSSC phytolith data enables the vegetation composition of the surrounding grassland to be assessed.

The oldest part of the analyzed sequence (Unit I, 10,380–6000 cal yr BP, Fig. 10), is characterized by sedimentation of minerogenic particles, low OM content and low accumulation rates. Between 10,380 and 8500 cal yr BP, the $\delta^{13}C_{bulk}$ value indicate mixed C_3 and C_4 vegetation existed in the local wetland (Fig. 10), with no occurrence of diatoms observed (Chapter 3.8). The C/N values show that the source of the OM was mainly terrestrial during the studied period, but lower values (<20) occurred between 9800 and 9140 cal yr BP, indicating that algae might have contributed to the matrix (Meyers, 1994) and that relatively mesic conditions prevailed initially (Unit Ia). The grain size distribution from the early part of this period was poorly sorted and dominated by fine particles, co-occurring with coarse sand. This is indicative of erosive conditions and enhanced fluvial activity (Table 4). Coarse silt dominated towards the end of the period. Around 8090 cal yr BP the C_3/C_4 index recorded the highest abundance of C_4 grasses, attributed to an increase of drought adapted C_4-Chloridoieae, indicating relatively dry conditions (Fig. 10). The $\delta^{13}C_{bulk}$ values are in line with these results, showing an increasing trend ca. 8000 cal yr BP, followed by a decline. The slow accumulation rates together with the low organic content suggest that prior to 7000 cal yr BP, the hydroclimatic conditions were relatively dry, at least seasonally, followed by erosion and deposition of relatively coarse material during the summer rainfall season.

From around 7000 cal yr BP, a general trend of increasing OM content (LOI, TOC, Fig. 10), together with an increase of the Panicoideae index and more depleted $\delta^{13}C_{bulk}$ values, are recorded. This suggests that moisture content was high enough to support organic accumulation due to increasing rainfall, and that C_3 (e.g. trees and shrub) vegetation likely contributed to the bulk organic matrix. The C/N values were generally elevated (>20), indicating that terrestrial input dominated the OM matrix. The grain size mode stayed around 20 μm, but increasing sand content was recorded around 5490 cal yr BP (Table 6), indicative of

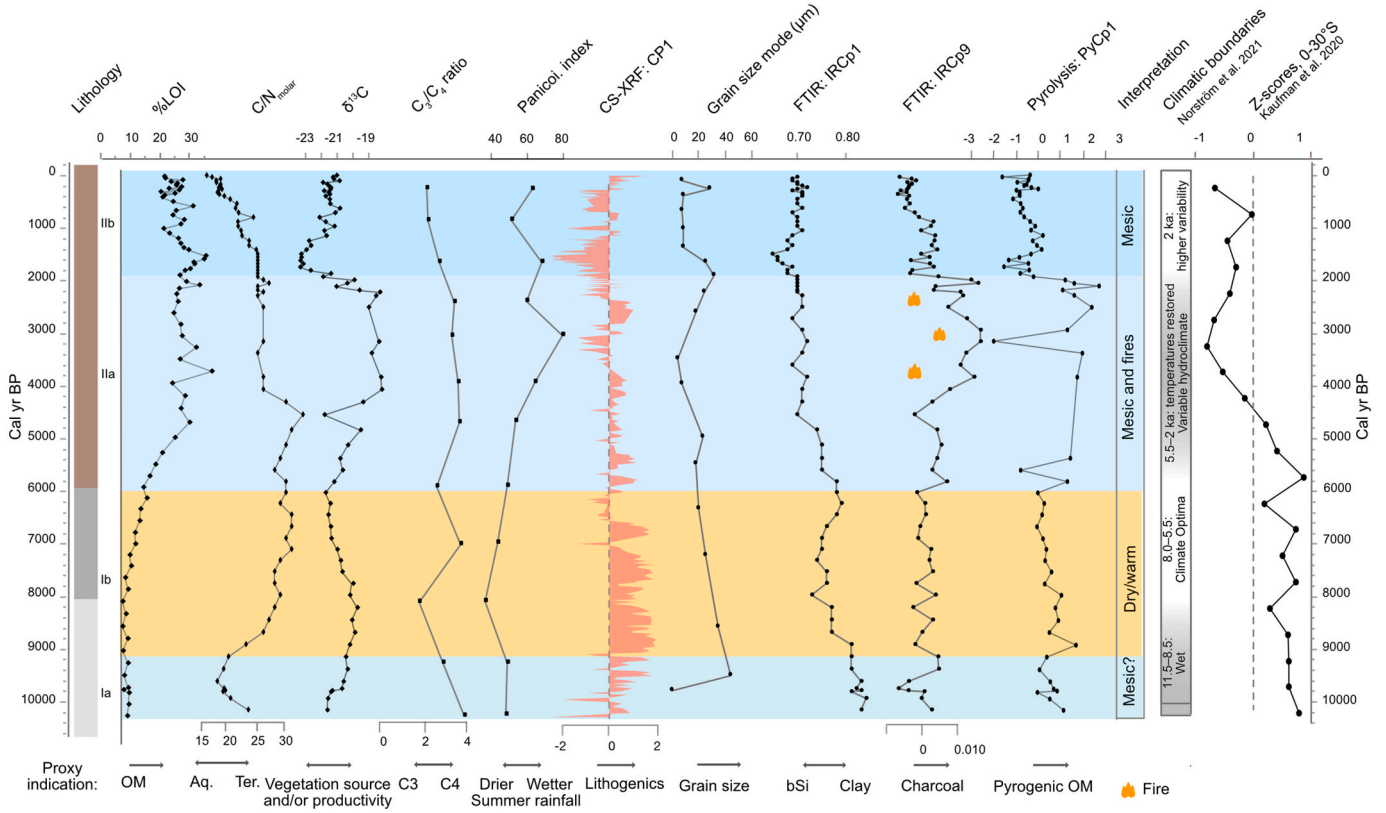

Fig. 10. Summary figure for Marais Geluk depicting proxy trends for source and organic matter content (%LOI, C/N, d^{13}C), grass composition (C_3/C_4 ratio and Panicoideae-index; note reversed axis for the *Ic*-index), lithogenic variability (XRFCp1) and grain size mode (μm). Two profiles were selected from the FTIR-ATR analysis, IRCp1 depicting variability of clay and bSi content. IRCp9 represents charcoal content, verified by PyCp1, increases (right) indicating increased fire incidence. Climate comparison with main chronostratigraphic units from Norström et al. (2021) and Holocene temperature trends (relative to the pre-industrial period) from the 12K database (v.0.54.0), a multi-method composite for the 0–30°S region, based on terrestrial proxies (Kaufman and et al., 2020).

an episodic increase in fluvial activity.

Early in Unit IIa, from ca. 6000 cal yr BP, OM accumulation accelerated, indicative of increasing accumulation and/or preservation of OM, while the Panicoideae index continued to increase until 3050 cal BP (Fig. 10). Between 4310 and 2180 cal yr BP, OM content is variable, but relatively high (>24% LOI, Fig. 10). The $\delta^{13}C_{bulk}$ values are also elevated, indicative of a dominance of C_4 litter in the OM matrix (−19‰). However, the phytolith data did not show any major shift between C_3 and C_4 grasses. This may indicate that $\delta^{13}C_{bulk}$ values during this period represented a non-grass vegetation, but a ^{13}C-enriched vegetation source, such as C_4 sedges (Finné et al., 2010; Norström et al., 2009; Stock et al., 2004) and/or aquatic OM (Smith and Walker, 1980).

During the last 2000 years (Unit IIb), relatively high OM content, accumulation rates and low $\delta^{13}C_{bulk}$ values were recorded. The phytolith indices showed that the occurrence of drought-adapted C_4 grasses was limited, indicating that relatively mesic conditions prevailed. Within this general trend, four periods of elevated organic content occurred centered around 1800, 800, 630 and 170 cal yr BP. The earlier of these periods (2050 and 1410 cal BP) was associated with the deposition of coarser particles (~30 μm), depleted $\delta^{13}C_{bulk}$ and predominantly C_4-Panicoideae. In contrast to previous periods, where higher OM content co-occurred with finer particles being deposited, the grain size data show that the sand content increased to around 18% (Table 6), indicating enhanced fluvial activity. Thereafter, the OM content and the Panicoideae index decreases until ca. 1000 cal yr BP, indicating drier conditions. Fine silt particles were deposited during this period. From 1000 to 190 cal yr BP increasing C_4 content is noted, both in the local wetland (elevated $\delta^{13}C_{bulk}$ values) and surrounding grassland (decreasing C_3/C_4 index, Fig. 10), while fine silt dominated the grain size distribution, except at 310 cal yr BP, when sand sized particles were deposited again, indicative of a brief period of enhanced fluvial activity.

4.2. *Geochemical characterization – interpretation of the PCA*

Three components captured 84% of the variance of the selected elements (Si, K, Ti, Rb, Mn, Sr, Ca, Y, Ga and Fe) (Table 2). Lithogenic elements were associated with the first component (XRFCp1: Si, K, Ti, Rb), indicating that XRFCp1 represents detrital minerogenic variability. The pXRD results show that the minerals occurring throughout the sequence were quartz (SiO_2), K-feldspar ($KAlSi_3O_8$) and plagioclase ($NaAlSi_3O_8$), together with minor occurrences of magnetite (Fe_2O_4) and anatase (TiO_2), supporting that the main variance of XRFCp1 is likely related to detrital mineral phases. Silica can also be associated to biogenic microfossils (diatoms, phytoliths), but the main association of Si to XRFCp1 suggests that most of the variance is related to changes in mineral matter content. Downcore variation of XRFCp1 (Fig. 5) shows that minerogenic sedimentation dominates in the oldest part of the sequence until 6530 cal yr BP, in line with the %LOI and TOC results. Furthermore, during the first 1000 years, the XRFCp1 increase was stepwise, which was not reflected in the other OM proxies. The grain size analysis from the oldest part of the sequence showed that finer grain sizes were deposited around 9770 cal yr BP compared to later periods, indicating that stepwise increase of XRFCp1 might reflect coarser particles being deposited. This is followed by a period of gradual increase in OM (Fig. 10: LOI, TOC) and decreasing mineral matter content. Increased lithogenic input is recorded between 6900 and 6600 cal yr BP, followed by generally lower values. Between 6000 and 3570 cal yr BP, overall lower XRFCp1 scores are observed, with oscillations around the average. After 3570 cal yr BP, mostly negative values are observed, with increases observed around 2810–2390, 910 and 850–700 cal yr BP.

When comparing periods of positive values to the grain size analysis data, we find that increased XRFCp1 values mostly correspond to coarser particles being deposited, as well as lower OM content (Fig. 10), suggesting that increased minerogenic input was associated to seasonally drier, more exposed soils and erosive conditions. An exception is noted between 2100 and 1500 cal yr BP, where high organic content (%LOI >25%) is associated with the deposition of coarser particles, as discussed further below (chapter 4.3). Most proxies indicate that the period following 2000 cal yr BP was variable but mostly mesic (higher OM content, increasing Panicoideae index, decreasing C/N).

The second component (XRFCp2) represents the main variance of Mn (strong positive association) together with a moderate contribution of the lithogenic elements (negative association). In wetland sequences, Mn can be hosted in primary minerals, oxides, colloids or bound to OM. The negative scores in the lowermost part of the sequence (<130 cm) together with the negative association of lithogenic elements to XRFCp2 suggest that Mn was here mainly associated with OM.

The third component (XRFCp3) includes a strong negative association with Fe and positive association with Ca and Sr. These elements are typically hosted in phases that are not stable in peat, such as iron oxides or carbonates (Malmer, 1988) or diffusion from underlying sediments (Steinmann and Shotyk, 1997), and thus likely depict an authigenic process and will not be used to interpret hydroclimatic variability.

4.3. FTIR and pyrolysis-GC-MS results related to the conventional proxies

The FTIR-ATR results support the inferences from the other inorganic and organic proxies (Fig. 3, Table 4), while also providing additional information on mineral, bSi and charcoal content (Fig. 10). The bSi content (IRCp2) to a large extent co-varied with the OM proxies (LOI, TOC, TN; Table 6), while the phytolith analysis showed that a majority of biogenic silica was related to plant remains (phytoliths) rather than diatoms. Component IRCp9 resembled the spectra for pyrogenic OM (charcoal), and independent analysis by pyrolysis-GC-MS confirmed that pyrogenic compounds (benzonitrile, naphthalene, biphenyl and fluorene) increased from 5820, peaked between 3800 and 1990, and co-occurred with elevated scores of IRCp9 (Fig. 10). These results show that FTIR-ATR analysis, with the aid of multivariate statistical analysis, can detect charcoal and, in turn, paleofire activity, in bulk wetland samples. During this period, increased charcoal content co-occurred with lowered TOC and TN content, while $\delta^{13}C_{bulk}$ values were elevated (~19‰, Fig. 10). A study by Sarangi et al. (2022) showed that fires may affect bulk organic proxies (TOC, $\delta^{13}C_{bulk}$ and other biomarker values), indicating that some of the observed co-occurrence at Marias Geluk between these variables may be related to fire-induced modification of the OM. The presence of pyrogenic OM, lowered TOC and accumulation rates during the period suggest that fires also reached the local wetland. However, the direction and magnitude of the increased $\delta^{13}C_{bulk}$ values (ca. +2‰) observed during the period indicates that a shift to a ^{13}C-enriched vegetation source also occurred, to for example C_4 sedges (Stock et al., 2004), C_4 grasses or aquatic OM (i.e., submerged aquatic plants using a HCO_3-based photosynthetic pathway) (Smith and Walker, 1980). To fully untangle the vegetation source, additional analyses are likely required, but the complex proxy responses during the period nevertheless show that increased fire activity may have profound effects, both on landscape vegetation composition (e.g. Cordova et al., 2019; Finch et al., 2022; Norström et al., 2014) and local wetland vegetation, paleoproxies and accumulation rates (this study).

4.4. Hydroclimate, vegetation and fire dynamics at Marais Geluk compared to regional paleo studies and paleoclimate

4.4.1. Early Holocene (ca. 10,000–8000 cal yr BP)

Terrestrial composite temperature reconstructions for 0–30°S show that, compared to pre-industrial conditions, the early Holocene was characterized by elevated temperatures that started to decline after 7000 cal yr BP (Kaufman and et al., 2020, Fig. 10). This is in line with the regional temperature reconstructions of Holmgren et al. (2003) and (Chevalier et al., 2021). Insolation changes for the region generally showed an opposite pattern (Kaufman and Broadman, 2023). Marine proxies, and more coastal sites (e.g Mfabeni peatland), depict a somewhat different temperature development, with a gradual increase in early Holocene until around 6000-5000 cal yr BP, after which temperaturea decreased (Chevalier and Chase, 2015; Fietz et al., 2023). Previous hydroclimatic reconstruction studies show that the early Holocene (ca. 11.5–8.5 ka cal BP) was characterized by relatively wet conditions in eastern South Africa (Combrink et al., 2022; Finné et al., 2010; Fitchett et al., 2016; Norström et al., 2014, 2021). A major wet phase was recorded at Ntsikeni wetland, KwaZulu-Natal (Combrink et al. (2022) around 10,000 cal yr BP, contemporary with sediment initiation at Marais Geluk.

In the initial parts of the Marais Geluk sequence, C/N values are low and fine grain sizes dominate, possibly indicating algal input to the organic matrix and presence of standing water. Also in the nearby Braamhoek wetland, relatively mesic conditions were inferred during this period (Finné et al., 2010; Norström et al., 2009, 2014), suggesting that increased wetness occurred at regional scale. After 9000 cal yr BP, C/N values increase again, indicating a shift towards increased terrestrial OM input, coarser particles were deposited and organic matter content was low, suggesting that relatively dry conditions prevailed, at least seasonally. The presence of relatively coarse particles (including coarse sand) indicates that either the dry conditions led to more exposed soils in the surrounding landscape, and thus more easily mobilized soil particles available for transport during the rainfall period. When turning to the organic proxies, the $\delta^{13}C_{bulk}$ and phytolith results suggest that a mixture of C_3 and C_4 vegetation existed both locally in the wetland and in the surrounding landscape, with a trend to drier summer conditions (decrease of C_4-Panicoideae) towards the mid-Holocene, indicating that the period was mostly dry.

4.4.2. Mid-to late Holocene (ca. 8000-2000 cal yr BP)

In the early mid-Holocene, during the climate optimum, elevated temperatures are reported in south-eastern Africa, peaking at different times depending on sites: around 8000 cal yr BP in Verloren vlei, Mpumalanga (Breman et al., 2019); between 7500 and 5500 cal yr BP in Ntsikeni wetland, KwaZulu-Natal (Combrink et al., 2022); and around 5000 cal yr BP at coastal peatland Mfabeni (Fietz et al., 2023). The composite climate reconstruction (Kaufman et al., 2020, Fig. 10) shows that temperatures were variable but generally high during the early mid-Holocene (8500–6000 cal yr BP), followed by a general decline towards 4000 cal yr BP. Paleo studies from the region report variable hydroclimatic conditions during this period, but several records initially report warm and wet conditions in the mid-Holocene (Norström et al., 2021, and references therein). At Marais Geluk, the phytolith indices suggest the driest conditions occurred around 8100 cal yr BP, followed by a trend towards increasingly mesic conditions and sedimentation of fine particles. Decreasing temperatures at Marais Geluk seem to have been paralleled by increasing bSi and OM content, indicating that increasingly mesic conditions prevailed in the local wetland.

From ca. 6000 cal yr BP, the ITCZ and associated monsoon systems were displaced south, which had large regional effects on precipitation patterns and caused the establishment of large desert areas in the Northern Hemisphere (e.g. Sahara, Gobi and Chichuan deserts) (Schneider et al., 2014; Wanner et al., 2008, 2011). Around 5500 cal yr BP, by the end of the African humid period, rapid climatic shifts have been recorded in several studies in south eastern Africa (Norström et al., 2021, Fig. 10). At Marais Geluk, no abrupt changes are noted, as most proxies (LOI, TOC, Panicoideae-index) rather depict a gradual trend towards increasingly mesic conditions (increasing OM and bSi content). Charcoal content started to increase from 5820 cal yr BP, indicating that increasingly mesic conditions co-occurred with higher fire incidence, possibly associated with increasing summer rainfall and influence of

tropical airmasses when the ITCZ moved southward. Around 5490 cal yr BP a peak in sand content was recorded (Table 6), indicating an episodic increase in fluvial activity. At Braamhoek wetland, proxy indicators suggest generally dry conditions between 6000 and 2000 cal yr BP, but the resolution of the sequence is low throughout this interval, limiting the possibilities to infer changes in hydroclimate (Finné et al., 2010; Norström et al., 2009, 2014).

A period of divergent proxy indications was observed between 4310 and 1990 cal yr BP. The C/N ratio decreased, pointing to a potential shift in the source of the OM. The $\delta^{13}C_{bulk}$ increased (−19‰), which could indicate a shift to C_4 litter in the OM matrix, while the grass phytolith data from this period showed no major changes in the distribution between C_3 and C_4 grasses (Fig. 10). Within the C_4 grasses, a shift towards dominance by the mesic adapted C_4-panicoideae is observed, however (Panicoideae index, Fig. 10). The OM content was relatively high (% LOI >24%), but TOC was somewhat suppressed compared to both the previous and following periods. The period was also associated with increasing charcoal content (Fig. 10), indicating increased fire activity. Similar trends in organic proxies and charcoal content were also recorded at Braamhoek wetland around this time (Norström et al., 2009), indicating that increased fire incidence was a regional phenomenon. The increase of the Panicoideae index, together with the relatively high organic content despite OM losses from local fires, indicate that relatively moist conditions prevailed, at least seasonally (Fig. 10). An alternative explanation is that the increased fire activity caused increased dust entrainment and deposition (Yu and Ginoux, 2022), so that the phytolith record during this period corresponded with a different transport process, and source area, compared to previous periods. However, deciphering shifts in the main transport process (e.g. from fluvial to aeolian), requires further study. Deposition of finer minerogenic particles was observed early in this phase compared to later. Overall, complex proxy responses seem to have occurred during this period that was characterized by overall cooler temperatures (Kaufman et al., 2020), relatively mesic conditions (increase in C_4-Panicoideae, relatively high OM content) and increased fire activity, as shown by elevated charcoal content (this study). An increase in fire incidence may explain some of the divergent proxy indications and the low sample resolution of the period, as seen both at Marais Geluk and Braamhoek wetlands (chapter 4.3, Sarangi et al., 2022).

4.4.3. *The last 2000 years*

During the last 2000 years, temperatures were variable, but mainly below the Holocene average (Kaufman et al., 2020, Fig. 10). A large number of paleo-climate reconstructions suggests greater climate variability in south-east Africa during the last 2000 years. The increased variability may be related to the higher resolution of records for the period, allowing short duration events to also be captured, and/or to increasing human activities affecting some of the proxies. At Marais Geluk, increased resolution (i.e., increasing accumulation rates) and variance between proxies are also recorded. Overall, elevated organic content, decreasing C/N values, deposition of fine silt particles, increasing C_4 vegetation and low charcoal content were observed at Marais Geluk during the last 2000 years, a trend that was reinforced after 900 cal yr BP (Fig. 10). Both the $\delta^{13}C_{bulk}$ and phytolith results depict increasing C_4 input to the organic matrix, and within the grass taxa this change was attributed to mesic adapted C_4-Panicoideae, supporting the notion that relatively mesic conditions prevailed. Within this general trend, four periods of increased organic content occurred, centered around 1800, 800, 630 and 170 cal yr BP. The first period (1900–1400 cal yr BP) was associated with deposition of coarser particles, the presence of diatoms, increasing bSi content, depleted $\delta^{13}C_{bulk}$ values and dominance by C_4-Panicoideae, indicating that mostly wet conditions prevailed. Low C/N values were observed from ca. 750 cal yr BP towards the present, indicating higher algal input to the organic matrix and increasingly wet conditions. The lower charcoal content observed during the period may be related to changes in biomass variability, lightning frequency or seasonality, climatic variability and/or human activities. Recent studies have shown that human activities may have affected fire regimes during the last 2000 years (Finch et al., 2022), by shifting of the fire seasonality to promote decreased fire intensity (pre-colonial) and overall fire suppression (colonial). Further studies are needed to untangle whether the decreased fire activity during the last 2000 years may be attributed to human activities, vegetation shifts or climatic variability for example by including micro-charcoal and pollen analyses, as well as additional ^{14}C dates to improve the chronological control of the record.

5. Conclusions

Multiproxy analysis was applied to a 175-cm wetland sequence from eastern Free State, South Africa. High resolution geochemical analysis was coupled with molecular, biogenic, grain size and mineral analyses. The inclusion of FTIR-ATR, pyrolysis-GC-MS and multivariate statistical analysis yielded greater insights into both the organic and inorganic properties of the sequence, and also enabled periods of increased charcoal content to be detected, interpreted as indicative of increased fire incidence. The chronological framework for these results was established through radiocarbon dating of bulk samples (n = 7). The Marais Geluk wetland sequence covers the last 10,380 years, and the earliest period, until ca. 7000 cal yr BP, was characterized by low organic content, slow accumulation rates and sedimentation of poorly sorted minerogenic particles. Elevated temperatures have been reconstructed for this period (12K database, Kaufman et al., 2020), which generally was associated with relatively dry conditions at Marais Geluk. From around 6000 cal yr BP temperatures decreased (Kaufman et al., 2020) and the ITCZ was displaced southward (Wanner et al., 2008), which at Marais Geluk was coupled to increased bSi and OM content while moisture adapted C_4-Paniocoideae expanded in the surrounding grassland, indicating a trend towards overall wetter conditions. Fire incidence likely started to increase from around 5800 cal yr BP, peaking between 4300 and 2180 cal yr BP. The increased fire activity, which also reached the local wetland, may explain both the low resolution of records from the region around this period, as well as the divergent trends observed in some proxies (e.g. $\delta^{13}C_{bulk}$ and GSSC phytolith results). The last 2000 years were mostly mesic with low fire incidence. Despite relatively limited temperature variations in sub-tropical areas during the Holocene (compared to northern higher latitudes), relatively large effects were observed at Marais Geluk throughout the Holocene, with relatively dry conditions, at least seasonally, observed during the early to mid Holocene, corroborating the conclusions from previous studies, as well as the IPCC report (Trisos et al., 2022), that current and future climate changes might have a profound impact on regional hydrology. The multiproxy approach applied here showed that complex proxy responses were recorded during periods of increased fire incidence, in particular for organic proxies, which might explain some of the observed divergent proxy responses noted during the late Holocene in eastern South Africa.

Author contribution

Jenny Sjöström: conceptualization, lead the writing of the paper, co-ordination of data collection and statistical processing, analysis (pXRD), supervision, fieldwork. **Antonio Martínez Cortizas**: co-ordination of FTIR and pyrolysis analysis, statistical processing, interpretation, funding acquisition, manuscript review and editing. **Andreas Nylund**: analysis (LOI, grain size), interpretations, manuscript review and editing. **Alice Hardman**: funding acquisition, analysis (phytolith) and interpretation, manuscript review and editing. **Joeri Kaal**: analysis (pyrolysis-GC-MS) and interpretation, manuscript review and editing. **Rienk Smittenberg**: analysis (C, N and δ13C) and interpretation, manuscript review and editing. **Jan Risberg**: fieldwork and phytolith preparation. **Daniel Schillereff**: interpretation, manuscript review and

editing. **Elin Norström**: conceptualization, analysis (^{14}C dating), co-ordination of sub-sampling and data analysis, funding acquisition, editing and reviewing.

Declaration of competing interest

The authors declare that they have no known competing financial interests or personal relationships that could have appeared to influence the work reported in this paper.

Data availability

The data is available for download at the Bolin Centre for Climate Research repository at https://bolin.su.se/data/sjostrom-2023-south-africa-1.

Acknowledgements

Mr Gideon Wessels, the landowner of the Marais Geluk farm and wetland, is thanked for guiding us to the wetland, the sampling permission and for participating in the field-work. Prof Rioual and two reviewers are thanked for thoughtful and valuable comments that helped to improve the manuscript. We are also grateful to Associate Professor Frank Neumann (North-West University, SA) and Dr Jemma Finch (University of KwaZulu-Natal, SA) for data and interpretation discussions. Dr Malin Kylander (Stockholm University, Sweden) is thanked for conducting the CS-XRF analysis, and providing interpretation guidance. Madalina Jaggi (ETH Zurich, Switzerland) is thanked for assistance with EA-IRMS analysis and Noelia River Chaver is thanked for conducting the FTIR-ATR (Universidad de Santiago de Compostela, Spain). E. Norström, J. Sjöström and A. Nylund were funded by the Swedish Research council (project no: 2019–05054). A. Hardman was funded by the European Molecular Biology Organization (grant no: 9703). The FTIR-ATR and pyrolysis-GC-MS analysis were funded by Grupos de Competitiva (ED431C 2021/32), Xunta de Galicia.

Appendix A. Supplementary data

Supplementary data to this article can be found online at https://doi.org/10.1016/j.quascirev.2023.108216.

References

Alexandre, A., Meunier, J.-D., Lézine, A.-M., Vincens, A., Schwartz, D., 1997. Phytoliths: indicators of grassland dynamics during the late Holocene in intertropical Africa. Palaeogeogr. Palaeoclimatol. Palaeoecol. 136, 213–229. https://doi.org/10.1016/S0031-0182(97)00089-8.

Álvarez Fernández, N., Martínez Cortizas, A., 2020. Andurinha: Make Spectroscopic Data Processing Easier.

Artz, R., Chapman, S., Campbell, C., 2006. Substrate utilisation profiles of microbial communities in peat are depth dependent and correlate with whole soil FTIR profiles. Soil Biol. Biochem. 38, 2958–2962. https://doi.org/10.1016/j.soilbio.2006.04.017.

Barboni, D., Bremond, L., 2009. Phytoliths of East African grasses: an assessment of their environmental and taxonomic significance based on floristic data. Rev. Palaeobot. Palynol. 158, 29–41. https://doi.org/10.1016/j.revpalbo.2009.07.002.

Battarbee, R.W., 1986. Diatom analysis. In: Handbook of Holocene Palaeoecology and Palaeohydrology. Wiley and Sons, Chichester, pp. 527–570.

Bertrand, S., Tjalingi, R., Malin Kylander, Wilhem, B., Brown, E., Roberts, S., Arnaud, F., Bindler, R., n.d.. Submitted. Inorganic Geochemistry of Lake Sediments. A Review of Analytical Techniques and Guidlines for Data Interpretation.

Biester, H., Knorr, K.-H., Schellekens, J., Basler, A., Hermanns, Y.-M., 2014. Comparison of different methods to determine the degree of peat decomposition in peat bogs. Biogeosciences 11, 2691–2707. https://doi.org/10.5194/bg-11-2691-2014.

Blaauw, M., Christen, J.A., 2011. Flexible paleoclimate age-depth models using an autoregressive gamma process. Bayesian Anal 6, 457–474. https://doi.org/10.1214/11-BA618.

Blott, S.J., Pye, K., 2001. GRADISTAT: a grain size distribution and statistics package for the analysis of unconsolidated sediments. Earth Surf. Process. Landforms 26, 1237–1248. https://doi.org/10.1002/esp.261.

Boggs, S., 2014. Sedimentary textures. In: Chapter 3, Sedimentology and Stratigraphy. Pearson Education Limited, Essex.

Breman, E., 2010. Pattern and Process in Grass-Dominated Ecosystems: Vegetation Dynamics at the Grassland-Savanna Ecotone in South-Africa during the Holocene (Doctoral Dissertation). University of Oxford, Oxford, UK.

Breman, E., Ekblom, A., Gillson, L., Norström, E., 2019. Phytolith-based environmental reconstruction from an altitudinal gradient in Mpumalanga, South Africa, 10,600 BP–present. Rev. Palaeobot. Palynol. 263, 104–116. https://doi.org/10.1016/j.revpalbo.2019.01.001.

Brindley, G.W., Brown, G., 1984. Crystal structures of clay mienrals and their X-ray identification. Mineral. Society, London.

Brown, E.T., Johnson, T.C., Scholz, C.A., Cohen, A.S., King, J.W., 2007. Abrupt change in tropical African climate linked to the bipolar seesaw over the past 55,000 years. Geophys. Res. Lett. 34, L20702 https://doi.org/10.1029/2007GL031240.

Chevalier, M., Chase, B.M., 2015. Southeast African records reveal a coherent shift from high- to low-latitude forcing mechanisms along the east African margin across last glacial–interglacial transition. Quat. Sci. Rev. 125, 117–130. https://doi.org/10.1016/j.quascirev.2015.07.009.

Chevalier, M., Chase, B.M., Quick, L.J., Dupont, L.M., Johnson, T.C., 2021. Temperature change in subtropical southeastern Africa during the past 790,000 yr. Geology 49, 71–75. https://doi.org/10.1130/G47841.1.

Combrink, M., Fitchett, J.M., Bamford, M.K., Botha, G.A., 2022. A late quaternary palaeoenvironmental record from Ntsikeni Wetland, KwaZulu-Natal Maloti-Drakensberg, South Africa. Quat. Int. 611–612, 55–65. https://doi.org/10.1016/j.quaint.2020.02.027.

Constantine, M., Mooney, S., Hibbert, B., Marjo, C., Bird, M., Cohen, T., Forbes, M., McBeath, A., Rich, A., Stride, J., 2021. Using charcoal, ATR FTIR and chemometrics to model the intensity of pyrolysis: exploratory steps towards characterising fire events. Sci. Total Environ. 783, 147052 https://doi.org/10.1016/j.scitotenv.2021.147052.

Cordova, C.E., 2023. Soil surface grass phytolith morphotypes across bioclimatic gradients and biomes at about latitude 29°S in South Africa. Rev. Palaeobot. Palynol. 313, 104887 https://doi.org/10.1016/j.revpalbo.2023.104887.

Cordova, C.E., 2013. C3 Poaceae and Restionaceae phytoliths as potential proxies for reconstructing winter rainfall in South Africa. Quat. Int. 287, 121–140. https://doi.org/10.1016/j.quaint.2012.04.022.

Cordova, C.E., Kirsten, K.L., Scott, L., Meadows, M., Lücke, A., 2019. Multi-proxy evidence of late-Holocene paleoenvironmental change at Princessvlei, South Africa: the effects of fire, herbivores, and humans. Quat. Sci. Rev. 221, 105896 https://doi.org/10.1016/j.quascirev.2019.105896.

Croudace, I.W., Löwemark, L., Tjallingii, R., Zolitschka, B., 2019. High resolution XRF core scanners: a key tool for the environmental and palaeoclimate sciences. Quat. Int. 514, 1–4. https://doi.org/10.1016/j.quaint.2019.05.038.

Davis, John.C., 2002. Statistics and Data Analysis in Geology, third ed. John Wiley & Sons, Toronto.

De la Rosa, J.M., Jiménez-González, M.A., Jiménez-Morillo, N.T., Knicker, H., Almendros, G., 2019. Quantitative forecasting black (pyrogenic) carbon in soils by chemometric analysis of infrared spectra. J. Environ. Manag. 251, 109567 https://doi.org/10.1016/j.jenvman.2019.109567.

Dean, W.E., 1974. Determination of carbonate and organic matter in calcareous sediments and sedimentary rocks by loss on ignition: comparison with other methods. SEPM J. Sediment. Res. 44 https://doi.org/10.1306/74D729D2-2B21-11D7-8648000102C1865D.

Degen, T., Sadki, M., Bron, E., König, U., Nénert, G., 2014. The HighScore suite. Powder Diffr. 29, S13–S18. https://doi.org/10.1017/S0885715614000840.

Diester-Haas, L., Schrader, H.J., Thiede, J., 1973. Sedimentological and paleoclimatological investigations of two pleagic ooze cores off Cape Barbas, North-West Africa. Geol. Geophys., Meteor Forsch-Ergebnisse: Reihe C. 16, 19–66.

Eisma, D., Van Der Gaast, S.J., 1971. Determination of opal in marine sediments by X-ray diffraction. Neth. J. Sea Res. 5, 382–389. https://doi.org/10.1016/0077-7579(71)90019-6.

Fietz, S., Baker, A., Miller, C.S., Naafs, B.D.A., Peterse, F., Finch, J., Humphries, M., Schefuß, E., Roychoudhury, A.N., Routh, J., 2023. Terrestrial temperature evolution of southern Africa during the late pleistocene and Holocene: evidence from the Mfabeni peatland. Quat. Sci. Rev. 299, 107870 https://doi.org/10.1016/j.quascirev.2022.107870.

Finch, J.M., Hill, T.R., 2008. A late Quaternary pollen sequence from Mfabeni Peatland, South Africa: reconstructing forest history in Maputaland. Quat. Res. 70, 442–450. https://doi.org/10.1016/j.yqres.2008.07.003.

Finch, J.M., Hill, T.R., Meadows, M.E., Lodder, J., Bodmann, L., 2022. Fire and montane vegetation dynamics through successive phases of human occupation in the northern Drakensberg, South Africa. Quat. Int. 611–612, 66–76. https://doi.org/10.1016/j.quaint.2021.01.026.

Finné, M., Norström, E., Risberg, J., Scott, L., 2010. Siliceous microfossils as late-Quaternary paleo-environmental indicators at Braamhoek wetland, South Africa. Holocene 20, 747–760. https://doi.org/10.1177/0959683610362810.

Fitchett, J.M., Grab, S.W., Bamford, M.K., Mackay, A.W., 2016. A multi-proxy analysis of late Quaternary palaeoenvironments, Sekhokong Range, eastern LesothoS. J. Quat. Sci. 31, 788–798. https://doi.org/10.1002/jqs.2902.

Fredlund, G.G., Tieszen, L.T., 1994. Modern phytolith assemblages from the north American great plains. J. Biogeogr. 21, 321. https://doi.org/10.2307/2845533.

Friedman, G.M., Sanders, J.E., 1978. Principles of Sedimentology. Wiley, New York.

Gendron-Badou, A., Coradin, T., Maquet, J., Fröhlich, F., Livage, J., 2003. Spectroscopic characterization of biogenic silica. J. Non-Cryst. Solids 316, 331–337. https://doi.org/10.1016/S0022-3093(02)01634-4.

Gosling, W.D., Cornelissen, H.L., McMichael, C.N.H., 2019. Reconstructing past fire temperatures from ancient charcoal material. Palaeogeogr. Palaeoclimatol. Palaeoecol. 520, 128–137. https://doi.org/10.1016/j.palaeo.2019.01.029.

Gray, A.B., Pasternack, G.B., Watson, E.B., 2010. Hydrogen peroxide treatment effects on the particle size distribution of alluvial and marsh sediments. Holocene 20, 293–301. https://doi.org/10.1177/0959683609350390.
Guo, Y., Bustin, R.M., 1998. FTIR spectroscopy and reflectance of modern charcoals and fungal decayed woods: implications for studies of inertinite in coals. Int. J. Coal Geol. 37, 29–53.
Hodgkins, S.B., Richardson, C.J., Dommain, R., Wang, H., Glaser, P.H., Verbeke, B., Winkler, B.R., Cobb, A.R., Rich, V.I., Missilmani, M., Flanagan, N., Ho, M., Hoyt, A. M., Harvey, C.F., Vining, S.R., Hough, M.A., Moore, T.R., Richard, P.J.H., De La Cruz, F.B., Toufaily, J., Hamdan, R., Cooper, W.T., Chanton, J.P., 2018. Tropical peatland carbon storage linked to global latitudinal trends in peat recalcitrance. Nat. Commun. 9, 3640. https://doi.org/10.1038/s41467-018-06050-2.
Hogg, A.G., Heaton, T.J., Hua, Q., Palmer, J.G., Turney, C.S., Southon, J., Bayliss, A., Blackwell, P.G., Boswijk, G., Bronk Ramsey, C., Pearson, C., Petchey, F., Reimer, P., Reimer, R., Wacker, L., 2020. SHCal20 southern Hemisphere calibration, 0–55,000 Years cal BP. Radiocarbon 62, 759–778. https://doi.org/10.1017/RDC.2020.59.
Holmes, P., Barker, C.H., 2006. Geological and geomorphological controls on the physical landscape of the free state. S. Afr. Geogr. J. 88, 3–10. https://doi.org/10.1080/03736245.2006.9713841.
Holmgren, K., Lee-Thorp, J.A., Cooper, G.R.J., Lundblad, K., Partridge, T.C., Scott, L., Sithaldeen, R., Siep Talma, A., Tyson, P.D., 2003. Persistent millennial-scale climatic variability over the past 25,000 years in Southern Africa. Quat. Sci. Rev. 22, 2311–2326. https://doi.org/10.1016/S0277-3791(03)00204-X.
Humphries, M., Green, A., Higgs, C., Strachan, K., Hahn, A., Pillay, L., Zabel, M., 2020. High-resolution geochemical records of extreme drought in southeastern Africa during the past 7000 years. Quat. Sci. Rev. 236, 106294 https://doi.org/10.1016/j.quascirev.2020.106294.
Humphries, M.S., 2021. Elemental proxy evidence for late Quaternary palaeoenvironmental change in southern African sedimentary records: interpretation and applications. S. Afr. J. Geol. 124, 1033–1046. https://doi.org/10.25131/sajg.124.0046.
Kaal, J., Brodowski, S., Baldock, J.A., Nierop, K.G.J., Cortizas, A.M., 2008. Characterisation of aged black carbon using pyrolysis-GC/MS, thermally assisted hydrolysis and methylation (THM), direct and cross-polarisation 13C nuclear magnetic resonance (DP/CP NMR) and the benzenepolycarboxylic acid (BPCA) method. Org. Geochem. 39, 1415–1426. https://doi.org/10.1016/j.orggeochem.2008.06.011.
Kaal, J., Gianotti, C., del Puerto, L., Criado-Boado, F., Rivas, M., 2019. Molecular features of organic matter in anthropogenic earthen mounds, canals and lagoons in the Pago Lindo archaeological complex (Tacuarembó, Uruguayan lowlands) are controlled by pedogenetic processes and fire practices. J. Archaeol. Sci. Rep. 26, 101900 https://doi.org/10.1016/j.jasrep.2019.101900.
Kaal, J., Martínez Cortizas, A., Nierop, K.G.J., 2009. Characterisation of aged charcoal using a coil probe pyrolysis-GC/MS method optimised for black carbon. J. Anal. Appl. Pyrolysis 85, 408–416. https://doi.org/10.1016/j.jaap.2008.11.007.
Kaufman, D., et al., 2020. A global database of Holocene paleotemperature records. Sci. Data 7, 34. https://doi.org/10.1038/s41597-020-0445-3.
Kaufman, D.S., Broadman, E., 2023. Revisiting the Holocene global temperature conundrum. Nature 614, 425–435. https://doi.org/10.1038/s41586-022-05536-w.
Krull, E.S., Skjemstad, J.O., Graetz, D., Grice, K., Dunning, W., Cook, G., Parr, J.F., 2003. 13C-depleted charcoal from C4 grasses and the role of occluded carbon in phytoliths. Org. Geochem. 34, 1337–1352. https://doi.org/10.1016/S0146-6380(03)00100-1.
Kylander, M.E., Ampel, L., Wohlfarth, B., Veres, D., 2011. High-resolution X-ray fluorescence core scanning analysis of Les Echets (France) sedimentary sequence: new insights from chemical proxies. J. Quat. Sci. 26, 109–117. https://doi.org/10.1002/jqs.1438.
Kylander, M.E., Holm, M., Fitchett, J., Grab, S., Martinez Cortizas, A., Norström, E., Bindler, R., 2021. Late glacial (17,060–13,400 cal yr BP) sedimentary and paleoenvironmental evolution of the Sekhokong Range (Drakensberg), southern Africa. PLoS One 16, e0246821. https://doi.org/10.1371/journal.pone.0246821.
Kylander, M.E., Martínez-Cortizas, A., Sjöström, J.K., Gåling, J., Gyllencreutz, R., Bindler, R., Alexanderson, H., Schenk, F., Reinardy, B.T.I., Chandler, B.M.P., Gallagher, K., 2023. Storm chasing: tracking Holocene storminess in southern Sweden using mineral proxies from inland and coastal peat bogs. Quat. Sci. Rev. 299, 107854 https://doi.org/10.1016/j.quascirev.2022.107854.
Lisztes-Szabó, Z., Kovács, S., Pető, Á., 2014. Phytolith analysis of Poa pratensis (Poaceae) leaves. Turk. J. Bot. 38, 851–863. https://doi.org/10.3906/bot-1311-8.
Löwemark, L., Bloemsma, M., Croudace, I., Daly, J.S., Edwards, R.J., Francus, P., Galloway, J.M., Gregory, B.R.B., Steven Huang, J.-J., Jones, A.F., Kylander, M., Löwemark, L., Luo, Y., Maclachlan, S., Ohlendorf, C., Patterson, R.T., Pearce, C., Profe, J., Reinhardt, E.G., Stranne, C., Tjallingii, R., Turner, J.N., 2019. Practical guidelines and recent advances in the Itrax XRF core-scanning procedure. Quat. Int. 514, 16–29. https://doi.org/10.1016/j.quaint.2018.10.044.
Malmer, N., 1988. Patterns in the growth and the accumulation of inorganic constituents in the sphagnum cover on ombrotrophic bogs in scandinavia. Oikos 53, 105. https://doi.org/10.2307/3565670.
Martínez Cortizas, A., López-Merino, L., Silva-Sánchez, N., Sjöström, J.K., Kylander, M. E., 2021a. Investigating the mineral composition of peat by combining FTIR-ATR and multivariate analysis. Minerals 11, 1084. https://doi.org/10.3390/min11101084.
Martínez Cortizas, A., Sjöström, J.K., Ryberg, E.E.S., Kylander, M.E., Kaal, J., López-Costas, O., Bindler, R., 2021b. 9000 years of change in peat organic matter composition in Store Mosse (Sweden) traced using FTIR-ATR. Boreas 50, 1161–1178. https://doi.org/10.1111/bor.12527.
Meyer-Jacob, C., Vogel, H., Boxberg, F., Rosén, P., Weber, M., Bindler, R., 2014. Independent measurment of biogenic silica in sediments by FTIR spectroscopy and PLS regression. J. Paleolimnol. 52, 245–255. https://doi.org/10.1007/s10933-014-9791-5.
Meyers, P.A., 1994. Preservation of elemental and isotopic source identification of sedimentary organic matter. Chem. Geol. 114, 289–302. https://doi.org/10.1016/0009-2541(94)90059-0.
Meyers, P.A., Ishiwatar, R., 1993. Lacustrine organic geochemistryman overview of indicators of organic matter sources and diagenesis in lake sediments. Org. Geochem. 20, 867–900.
Miller, C., Finch, J., Hill, T., Peterse, F., Humphries, M., Zabel, M., Schefuß, E., 2019. Late Quaternary climate variability at Mfabeni peatland, eastern South Africa. Clim. Past 15, 1153–1170. https://doi.org/10.5194/cp-15-1153-2019.
Moore, M.D., Reynolds, C.R., 1997. X-Ray Diffraction and the Identification and Analysis of Clay Minerals, second ed. Oxford University Press, Oxford, UK.
Moreno, A., Giralt, S., Valero-Garcés, B., Sáez, A., Bao, R., Prego, R., Pueyo, J.J., González-Sampériz, P., Taberner, C., 2007. A 14kyr record of the tropical Andes: the Lago Chungará sequence (18°S, northern Chilean Altiplano). Quat. Int. 161, 4–21. https://doi.org/10.1016/j.quaint.2006.10.020.
Moreno, A., Valero-Garcés, B.L., González-Sampériz, P., Rico, M., 2008. Flood response to rainfall variability during the last 2000 years inferred from the Taravilla Lake record (Central Iberian Range, Spain). J. Paleolimnol. 40, 943–961. https://doi.org/10.1007/s10933-008-9209-3.
Mucina, L., Rutherford, M.C., 2006. The Vegetation of South Africa, Lesotho and Swaziland. South African National Biodiversity Institute, Pretoria.
Müller, C.M., Pejcic, B., Esteban, L., Piane, C.D., Raven, M., Mizaikoff, B., 2014. Infrared attenuated total reflectance spectroscopy: an innovative strategy for analyzing mineral components in energy relevant systems. Sci. Rep. 4, 6764. https://doi.org/10.1038/srep06764.
Neumann, K., Strömberg, C.A.E., Ball, T., Albert, R.M., Vrydaghs, L., Cummings, L.S., 2019. International code for phytolith nomenclature (ICPN) 2.0. Ann. Bot. 124, 189–199. https://doi.org/10.1093/aob/mcz064.
Norström, E., Kylander, M.E., Sitoe, S.R., Finch, J.M., 2021. Chronostratigraphic palaeoclimate phasing based on southern African wetlands: from the escarpment to the eastern seaboard. S. Afr. J. Geol. 124, 977–994. https://doi.org/10.25131/sajg.124.0063.
Norström, E., Neumann, F.H., Scott, L., Smittenberg, R.H., Holmstrand, H., Lundqvist, S., Snowball, I., Sundqvist, H.S., Risberg, J., Bamford, M., 2014. Late Quaternary vegetation dynamics and hydro-climate in the Drakensberg, South Africa. Quat. Sci. Rev. 105, 48–65. https://doi.org/10.1016/j.quascirev.2014.09.016.
Norström, E., Scott, L., Partridge, T.C., Risberg, J., Holmgren, K., 2009. Reconstruction of environmental and climate changes at Braamhoek wetland, eastern escarpment South Africa, during the last 16,000 years with emphasis on the Pleistocene–Holocene transition. Palaeogeogr. Palaeoclimatol. Palaeoecol. 271, 240–258. https://doi.org/10.1016/j.palaeo.2008.10.018.
Novello, A., Bamford, M.K., Van Wijk, Y., Wurz, S., 2018. Phytoliths in modern plants and soils from Klasies river, Cape region (South Africa). Quat. Int. 464, 440–459. https://doi.org/10.1016/j.quaint.2017.10.009.
Novello, A., Barboni, D., Berti-Equille, L., Mazur, J.-C., Poilecot, P., Vignaud, P., 2012. Phytolith signal of aquatic plants and soils in Chad, Central Africa. Rev. Palaeobot. Palynol. 178, 43–58. https://doi.org/10.1016/j.revpalbo.2012.03.010.
Reimer, P., Brown, T., Reimer, R., 2004. Discussion: reporting and calibration of post-bomb ^{14} C data. Radiocarbon 46, 1299–1304. https://doi.org/10.1017/S0033822200033154.
Reimer, R.W., Reimer, P.J., 2022. CALIBomb.
Rossouw, L., 2009. The Application of Fossil Grass-Phytolith Analysis in the Reconstruction of Late Cainozoic Environments in the South African Interior (Doctoral Thesis). University of the Free State, Bloemfontein, South Africa.
Sarangi, V., Roy, S., Sanyal, P., 2022. Effect of burning on the distribution pattern and isotopic composition of plant biomolecules: implications for paleoecological studies. Geochem. Cosmochim. Acta 318, 305–327. https://doi.org/10.1016/j.gca.2021.12.003.
Schneider, T., Bischoff, T., Haug, G.H., 2014. Migrations and dynamics of the intertropical convergence zone. Nature 513, 45–53. https://doi.org/10.1038/nature13636.
Scott, L., Holmgren, K., Talma, S., Woodborne, S., Vogel, J., 2003. Age interpretation of the Wonderkrater spring sediments and vegetation change in the Savanna. South Afr. J. Sci. 99, 484–488.
Scott, L., Lee-Thorp, J.A., 2004. Holocene climatic trends and rhythms in southern Africa. In: Battarbee, R.W., Gasse, F., Stickley, C.E. (Eds.), Past Climate Variability through Europe and Africa, Developments in Paleoenvironmental Research. Springer Netherlands, Dordrecht, pp. 69–91. https://doi.org/10.1007/978-1-4020-2121-3_5.
Sjöström, J., Norström, E., Risberg, J., Schoeman, M.H., 2017. Late Holocene palaeoenvironmental reconstruction from Mpumalanga Province (South Africa) inferred from geochemical and biogenic proxies. Rev. Palaeobot. Palynol. 246, 264–277. https://doi.org/10.1016/j.revpalbo.2017.06.011.
Sjöström, J.K., Bindler, R., Granberg, T., Kylander, M.E., 2019. Procedure for organic matter removal from peat samples for XRD mineral analysis. Wetlands 39, 473–481. https://doi.org/10.1007/s13157-018-1093-7.
Smith, F.A., Walker, N.A., 1980. Photosynthesis by aquatic plants: effects of unstirred layers in relation to assimilation of CO2 and HCO3- and to carbon isotopic discriminiation. New Phytol. Trust 86, 245–259.
South African National Biodiversity Institute, 2018. 2018 Final Vegetation Map of South Africa, Lesotho and Swaziland.
Steinmann, P., Shotyk, W., 1997. Geochemistry, mineralogy, and geochemical mass balance on major elements in two peat bog profiles (Jura Mountains, Switzerland). Chem. Geol. 138, 25–53. https://doi.org/10.1016/S0009-2541(96)00171-4.

Stock, W.D., Chuba, D.K., Verboom, G.A., 2004. Distribution of South African C3 and C4 species of Cyperaceae in relation to climate and phylogeny. Austral Ecol. 29, 313–319. https://doi.org/10.1111/j.1442-9993.2004.01368.x.

Swann, G.E.A., Patwardhan, S.V., 2011. Application of Fourier Transform Infrared Spectroscopy (FTIR) for assessing biogenic silica sample purity in geochemical analyses and palaeoenvironmental research. Clim. Past 7, 65–74. https://doi.org/10.5194/cp-7-65-2011.

Tinti, A., Tugnoli, V., Bonora, S., Francioso, O., 2015. Recent applications of vibrational mid-Infrared (IR) spectroscopy for studying soil components: a review. J. Cent. Eur. Agric. 16, 1–22. https://doi.org/10.5513/JCEA01/16.1.1535.

Tooth, S., McCarthy, T.S., 2007. Wetlands in drylands: geomorphological and sedimentological characteristics, with emphasis on examples from southern Africa. Prog. Phys. Geogr. Earth Environ. 31, 3–41. https://doi.org/10.1177/0309133307073879.

Trisos, C.H., Adelekan, I.O., Totin, E., Ayanlade, A., Efitre, J., Gemeda, A., Kalaba, K., 2022. Africa. Clim. Change 2022 Impact Adapt. Vulnerability Contributions of Working Group II to the Sixth Assessment Report of the Intergovernmental Panel on Climate Change, pp. 1285–1455. https://doi.org/10.1017/9781009325844.01.

Tsoar, H., Pye, K., 1987. Dust transport and the question of desert loess formation. Sedimentology 34, 139–153. https://doi.org/10.1111/j.1365-3091.1987.tb00566.x.

Turney, C.S.M., Wheeler, D., Chivas, A.R., 2006. Carbon isotope fractionation in wood during carbonization. Geochem. Cosmochim. Acta 70, 960–964. https://doi.org/10.1016/j.gca.2005.10.031.

Twiss, P.C., 1992. Predicted word distribution of C3 and C4 grass phytoliths. In: Phytolith Systematics - Emerging Issues. Plenum Press, New York, pp. 113–128.

Twiss, P.C., Suess, E., Smith, R.M., 1969. Morphological classificatio of grass phytoliths. Proc. Soil Sci. Soc. Am. 109–1115.

Vandenberghe, J., 2013. Grain size of fine-grained windblown sediment: a powerful proxy for process identification. Earth Sci. Rev. 121, 18–30. https://doi.org/10.1016/j.earscirev.2013.03.001.

Vogel, J.C., Fuls, A., Ellis, R.P., 1978. The geographical distribution of Kranz grasses in South Africa. S. Afr. J. Sci. 74: 209-215. South Afr. J. Sci. 74, 209–215.

Wanner, H., Beer, J., Bütikofer, J., Crowley, T.J., Cubasch, U., Flückiger, J., Goosse, H., Grosjean, M., Joos, F., Kaplan, J.O., Küttel, M., Müller, S.A., Prentice, I.C., Solomina, O., Stocker, T.F., Tarasov, P., Wagner, M., Widmann, M., 2008. Mid- to Late Holocene climate change: an overview. Quat. Sci. Rev. 27, 1791–1828. https://doi.org/10.1016/j.quascirev.2008.06.013.

Wanner, H., Solomina, O., Grosjean, M., Ritz, S.P., Jetel, M., 2011. Structure and origin of Holocene cold events. Quat. Sci. Rev. 30, 3109–3123. https://doi.org/10.1016/j.quascirev.2011.07.010.

Weltje, G.J., Bloesma, M.R., Tjallingi, R., Heslop, U., Croudace, I.W., 2015. Prediction of geochemical composition from XRF core scanner data: a new multivariate approach including automatic selection of calibration samples and quantification of uncertainties. In: Micro-XRF Studies of Sediment Cores, Developments in Paleoenvironmental Research. Springer, Dordrecht, pp. 507–534.

Yancheva, G., Nowaczyk, N.R., Mingram, J., Dulski, P., Schettler, G., Negendank, J.F.W., Liu, J., Sigman, D.M., Peterson, L.C., Haug, G.H., 2007. Influence of the intertropical convergence zone on the East Asian monsoon. Nature 445, 74–77. https://doi.org/10.1038/nature05431.

Yu, Y., Ginoux, P., 2022. Enhanced dust emission following large wildfires due to vegetation disturbance. Nat. Geosci. 15, 878–884. https://doi.org/10.1038/s41561-022-01046-6.

Zegouagh, Y., Derenne, S., Dignac, M.F., Baruiso, E., Mariotti, A., Largeau, C., 2004. Demineralisation of a crop soil by mild hydrofluoric acid treatment. J. Anal. Appl. Pyrolysis 71, 119–135. https://doi.org/10.1016/S0165-2370(03)00059-7.